Monthly Notices
of the
ROYAL ASTRONOMICAL SOCIETY

MNRAS **461,** 4295–4316 (2016)
Advance Access publication 2016 July 7

doi:10.1093/mnras/stw1626

Dark matter concentrations in galactic nuclei according to polytropic models

Curtis J. Saxton,[1]★ Ziri Younsi[2]★ and Kinwah Wu[3]★

[1]*Physics Department, Technion – Israel Institute of Technology, Haifa 32000, Israel*
[2]*Institut für Theoretische Physik, Max-von-Laue-Straße 1, D-60438 Frankfurt am Main, Germany*
[3]*Mullard Space Science Laboratory, University College London, Holmbury St Mary, Surrey RH5 6NT, UK*

Accepted 2016 July 5. Received 2016 June 24; in original form 2015 November 30

ABSTRACT

We calculate the radial profiles of galaxies where the nuclear region is self-gravitating, consisting of self-interacting dark matter (SIDM) with F degrees of freedom. For sufficiently high density this dark matter becomes collisional, regardless of its behaviour on galaxy scales. Our calculations show a spike in the central density profile, with properties determined by the dark matter microphysics, and the densities can reach the 'mean density' of a black hole (from dividing the black hole mass by the volume enclosed by the Schwarzschild radius). For a galaxy halo of given compactness ($\chi \equiv 2GM/Rc^2$), certain values for the dark matter entropy yield a dense central object lacking an event horizon. For some soft equations of state of the SIDM (e.g. $F \gtrsim 6$), there are multiple horizonless solutions at given compactness. Although light propagates around and through a sphere composed of dark matter, it is gravitationally lensed and redshifted. While some calculations give non-singular solutions, others yield solutions with a central singularity. In all cases, the density transitions smoothly from the central body to the dark matter envelope around it, and to the galaxy's dark matter halo. We propose that pulsar timing observations will be able to distinguish between systems with a centrally dense dark matter sphere (for different equations of state) and conventional galactic nuclei that harbour a supermassive black hole.

Key words: black hole physics – pulsars: general – galaxies: haloes – galaxies: nuclei – dark matter.

1 INTRODUCTION

Invisibly compact, relativistic objects appear to reside in the central regions of most large galaxies. Their masses appear to correlate with certain host properties (e.g. Magorrian et al. 1998; Ferrarese & Merritt 2000; Laor 2001; Häring & Rix 2004; Feoli & Mancini 2009; Gültekin et al. 2009; Burkert & Tremaine 2010; Graham et al. 2011; Soker & Meiron 2011; Xiao et al. 2011; Rhode 2012; Bogdán & Goulding 2015; Ginat, Meiron & Soker 2016). If these objects are dense enough to possess an event horizon, then they are supermassive black holes (SMBH). More exotic alternatives may lack a horizon (e.g Müller Zum Hagen, Yodzis & Seifert 1974; Ori & Piran 1987; Tkachev 1991; Viollier, Trautmann & Tupper 1993; Tsiklauri & Viollier 1998; Schunck & Torres 2000; Kovács & Harko 2010; Joshi, Malafarina & Narayan 2011; Diemer et al. 2013; Meliani et al. 2015). Whatever they are, some of these nuclei act as 'quasars' during episodes of bright, rapid gas accretion. Powerful quasars are found at high redshifts (e.g. Fan et al. 2004; Mortlock et al. 2011; Venemans et al. 2013; Ghisellini et al. 2015; Wu et al. 2015), implying that their central objects were already present and grew on short time-scales in the early Universe. The largest ultramassive black hole candidates are a few $10^{10}\,\mathrm{m}_\odot$ (McConnell et al. 2011; Postman et al. 2012; van den Bosch et al. 2012; Fabian et al. 2013; Shields & Bonning 2013; Ghisellini et al. 2015; Yıldırım et al. 2015, 2016; Scharwächter et al. 2016; Thomas et al. 2016). These are difficult to reconcile with the conventional scenario in which SMBH grew via accretion of luminous gas and stars (Soltan 1982; Yu & Tremaine 2002; Shankar, Weinberg & Miralda-Escudé 2009; Novak 2013).

Galaxies possess another significant non-luminous component, in the form of invisible 'dark matter' (DM) that seems to reside in spheroidal haloes: more radially extended than the visible matter (Oort 1932; Zwicky 1937; Babcock 1939; Ostriker & Peebles 1973). The fundamental nature of DM is unknown, besides constraints on its electromagnetic traits (e.g. Sigurdson et al. 2004; McDermott, Yu & Zurek 2011; Cline, Moore & Frey 2012; Kadota & Silk 2014; Khlopov 2014). Cosmic filaments and voids can form in collisionless cold dark matter (CDM; e.g. Frenk, White & Davis 1983; Melott et al. 1983; Springel, Frenk & White 2006), self-interacting dark fluid (Moore et al. 2000), or wavelike cosmic boson

★E-mail: saxton@physics.technion.ac.il (CJS); younsi@th.physik.uni-frankfurt.de (ZY); kinwah.wu@ucl.ac.uk (KW)

fields (Woo & Chiueh 2009; Schive, Chiueh & Broadhurst 2014a; Schive et al. 2014b). However, when simulations treat the DM like a collisionless gravitating dust, steep power-law density cusps emerge throughout the centres of self-bound systems (Gurevich & Zybin 1988; Dubinski & Carlberg 1991; Navarro, Frenk & White 1996). Observationally, at kiloparsec scales, DM in most types of galaxies exhibits nearly uniform central *cores* that attenuate at larger radii (e.g. Flores & Primack 1994; Moore 1994; Burkert 1995; Salucci & Burkert 2000; Gentile et al. 2004; Gilmore et al. 2007; Oh et al. 2008; Herrmann & Ciardullo 2009; Inoue 2009; de Blok 2010; Saxton & Ferreras 2010; Memola, Salucci & Babić 2011; Walker & Peñarrubia 2011; Agnello & Evans 2012; Lora et al. 2012, 2013; Salucci et al. 2012; Schuberth et al. 2012; Amorisco, Agnello & Evans 2013; Bottema & Pestaña 2015; Pota et al. 2015). Among many interpretations, it has been suggested that the dark cores are supported by dark pressure due to DM self-interactions via self-scattering, longer range dark forces, or more exotic mechanisms (e.g. Peebles 2000; Spergel & Steinhardt 2000; Ackerman et al. 2009; Boddy et al. 2014; Cline et al. 2014b; Hochberg et al. 2014; Heikinheimo et al. 2015). If self-interacting dark matter (SIDM) is in this sense plasma- or gas-like, then the manner of its interaction with the SMBH (or other exotic central object) could provide informative constraints on the physics of both these mysterious entities.

While a realistic halo should be cored at kpc scales, dense concentrations of visible matter exert a gravitational influence that may steepen the innermost part of the DM profile: 'adiabatic contraction' of collisionless DM (Blumenthal et al. 1986; Gnedin et al. 2004), or SIDM (Saxton 2013, fig. 1). A central massive object could distort the innermost parts of the halo, forming a dark density 'spike' within the local sphere of influence (Huntley & Saslaw 1975; Quinlan, Hernquist & Sigurdsson 1995; Munyaneza & Biermann 2005; Guzmán & Lora-Clavijo 2011b,a). This DM substructure might continue to grow denser near an SMBH's event horizon. Relaxation processes and star formation in galaxy nuclei can grow power-law stellar density cusps (e.g. Bahcall & Wolf 1976, 1977; Freitag, Amaro-Seoane & Kalogera 2006; Alexander & Hopman 2009; Aharon & Perets 2015), which could also help to induce a dark spike. Scattering by stars would render the DM indirectly collisional, regardless of its collisionality in the rarefied outskirts of haloes (Ilyin, Zybin & Gurevich 2004; Merritt 2004, 2010).

The most commonly predicted spike profile is $\rho \sim r^{-3/2}$. For DM with F thermal degrees of freedom (and an adiabatic pressure–density law $P \propto \rho^{(F+2)/F}$), the spike profile tends to $\rho \sim r^{-F/2}$ in Newtonian regions (far outside any event horizon). This is the maximum slope when the central mass dominates DM self-gravity. (In regions where DM self-gravity is more influential than the central mass, density gradients can be locally shallow; and concentric regions can alternate between steep and shallow, as we describe in subsection 3.2.) If SIDM consists of particles scattering with a velocity-dependent cross-section ($\varsigma \propto v^{-a}$) then the ratio of mean free path to radial position is $l/r \sim r^{(F-a-2)/2}$ in the spike.[1] If the heat capacity is high ($F > 6$, a 'soft' equation of state) then l shortens enough at small radii that the centre is maximally collisional, for microphysics ranging from hard spheres ($a = 0$) to Coulomb scattering ($a = 4$). The possibility of centrally strengthening SIDM interactions has so far not been considered in papers that implicitly assumed $F = 3$, (e.g. Shapiro & Paschalidis 2014). It is worth emphasizing that *collisional* pressure is not the only conceivable type of interaction. For instance, a dark plasma might be mediated by a dark version of electromagnetism, and develop collisionless shocks like ionized plasmas do (e.g. Ackerman et al. 2009; Heikinheimo et al. 2015). Boson condensate and scalar field DM theories entail effective pressures due to quantum effects (e.g. Goodman 2000; Peebles 2000; Arbey, Lesgourgues & Salati 2003; Böhmer & Harko 2007; Chavanis & Delfini 2011; Harko 2011a,b; Robles & Matos 2012; Meliani et al. 2015). Fermionic DM could exhibit degeneracy pressure (e.g. Munyaneza & Biermann 2005; Destri, de Vega & Sanchez 2013; de Vega & Sanchez 2014; Horiuchi et al. 2014; Domcke & Urbano 2015; Kouvaris & Nielsen 2015).

At galaxy scales, early simulations of weakly scattering, thermally conductive SIDM predicted unrealistic steeper cusps, forming via gravothermal catastrophe (e.g. Burkert 2000; Kochanek & White 2000). More detailed investigations defer this collapse to the far cosmological future, and show the existence of another plausible regime in which strong scattering (short mean free paths) inhibits conduction and enables adiabatic, fluid-like phenomena (Balberg, Shapiro & Inagaki 2002; Ahn & Shapiro 2005; Koda & Shapiro 2011).

Much recent research concentrated on the conjecture that DM is a weakly interacting massive particle with cosmologically long self-scattering time-scales (e.g. Buckley & Fox 2010; Feng, Kaplinghat & Yu 2010; Loeb & Weiner 2011). These models raise hopes of detecting DM decay or annihilation by-products from the central spike (e.g. Gondolo & Silk 1999; Merritt 2004, 2010). In most of these models, the DM particles are point-like and lack substructure (possessing only translational degrees of freedom, $F = 3$). This can be implemented in N-body simulations with infrequent Monte Carlo scattering. Some simulations predict overly large SIDM cores, which prompted suggestions that the scattering cross-section is small or velocity dependent ($\varsigma < 1\,\mathrm{cm}^2\,\mathrm{g}^{-1}$, e.g. Yoshida et al. 2000; Davé et al. 2001; Arabadjis, Bautz & Garmire 2002; Katgert, Biviano & Mazure 2004; Vogelsberger, Zavala & Loeb 2012; Peter et al. 2013; Rocha et al. 2013; Elbert et al. 2015). Alternatively, SIDM may have a higher internal heat capacity ($F > 3$). Without restricting the scattering physics, analytic models show that the range of $7 \lesssim F < 10$ results in galaxy clusters with realistic $\sim 10^1$–10^2 kpc cores (Saxton & Wu 2008, 2014), while the range $7 \lesssim F \lesssim 9$ can fit elliptical galaxy kinematics (Saxton & Ferreras 2010) and naturally provides the observed scaling relations between galaxies and their SMBH (Saxton et al. 2014). Isolated galaxies gain dynamical stability from a suitable concentration of collisionless stars permeating the SIDM halo (Saxton 2013).

Within this rich diversity of DM theories, it is interesting to investigate whether there might be any direct relationship between SIDM and SMBH, enabling falsifiable predictions about one or the other. DM might contribute significantly to the origin and growth of SMBH. Ostriker (2000) and Hennawi & Ostriker (2002) assumed an initially cuspy profile with weakly interacting SIDM, and inferred that collisionality must be weak in order to prevent SMBH from growing larger than observed. Balberg & Shapiro (2002) began with a cored SIDM profile, and showed that some versions of SIDM (with $F = 3$) could form realistic SMBH and halo cores, prior to gravothermal catastrophe in some future era. Other fluid-like accretion models (in various contexts, with or without self-gravity) affirm that DM could contribute significantly to SMBH growth (e.g. MacMillan & Henriksen 2002; Munyaneza & Biermann 2005; Richter, Tupper & Viollier 2006; Hernandez & Lee 2010; Guzmán & Lora-Clavijo 2011b,a; Pepe, Pellizza & Romero 2012; Lora-Clavijo, Gracia-Linares & Guzman 2014). In galaxy cluster models, combining DM with radiative gas (Saxton & Wu 2008, 2014),

[1] For any a, and fixing a sign in Saxton, Soria & Wu (2014) p. 3427.

the physically consistent solutions always have a compact central mass.

In the fully relativistic theory of self-gravitating spherical accretion, accretion rates are maximal when the surrounding fluid envelope is half the mass of the accretor (Karkowski et al. 2006; Mach 2009). This condition assumes special cases with a sonic point in the flow. Alternative, entirely subsonic solutions might be longer lived, with relatively more massive fluid envelopes. It is conceivable that hydrostatic pressure might support a near-stationary SIDM envelope around a black hole. This paper will focus on scenarios in which a quasi-static SIDM spike is itself relativistically dense and supermassive. For now, we set aside the complications of gaseous and stellar physics, and appraise the effects of a spike of SIDM at densities comparable to the black hole, in regions all the way down to the event horizon. We will also see that an SMBH (with an event horizon) can be entirely replaced by an SIDM condensate.

2 MODEL

2.1 Formulation

The interval between events within and around a spherical mass distribution is $\mathrm{d}\lambda = -c\,\mathrm{d}\tau$, with the proper time τ given by

$$c^2\mathrm{d}\tau^2 = c^2\mathrm{e}^{2\Phi}\mathrm{d}t^2 - \frac{r\,\mathrm{d}r^2}{r-h} - r^2\left(\mathrm{d}\theta^2 + \sin^2\theta\,\mathrm{d}\phi^2\right)\,, \tag{1}$$

in spherical coordinates (t, r, ϕ, θ). Here, r is the radius at a surface of circumference $2\pi r$, and $\Phi = \Phi(r)$ is a dimensionless gravitational potential. We abbreviate $h \equiv 2Gm/c^2$ for the Schwarzschild radius of the enclosed gravitating mass, $m = m(r)$. We seek solutions of the Tolman–Oppenheimer–Volkoff ('TOV'; Tolman 1934, 1939; Oppenheimer & Volkoff 1939) model for a hydrostatic self-gravitating sphere. Unlike those classic models of relativistic stars, we allow a singularity or event horizon to occur at some inner radius $r_\dagger$ (which will be obtained numerically). At each radius r, there is locally an isotropic pressure P and energy density ϵ. These quantities are linked by coupled differential equations,

$$\frac{\mathrm{d}m}{\mathrm{d}r} = 4\pi r^2\epsilon/c^2 \geq 0\,, \tag{2}$$

$$\frac{\mathrm{d}\Phi}{\mathrm{d}r} = \frac{G(m + 4\pi r^3 P/c^2)}{c^2 r(r-h)} \geq 0\,, \tag{3}$$

$$\frac{\mathrm{d}P}{\mathrm{d}r} = -\frac{G(m + 4\pi r^3 P/c^2)(\epsilon + P)}{c^2 r(r-h)} = -(\epsilon + P)\frac{\mathrm{d}\Phi}{\mathrm{d}r} \leq 0\,. \tag{4}$$

We seek solutions with finite total mass (M) within an outer boundary ($r = R$) where the density vanishes ($\epsilon \to 0$). At this boundary the potential matches that of the external Schwarzschild (1916) vacuum model:

$$\Phi_{_R} = \frac{1}{2}\ln\left(1 - \frac{2GM}{c^2 R}\right)\,. \tag{5}$$

The total energy density includes rest-mass density (ρ) and internal energy components,

$$\epsilon = \rho c^2 + \frac{FP}{2}\,, \tag{6}$$

where F is the number of effective thermal degrees of freedom, which depends on the DM microphysics. In this paper, we assume that F is spatially constant. If the DM behaves adiabatically then there is a polytropic[2] equation of state,

$$P = \rho\sigma^2 = s\rho^\gamma\,, \tag{7}$$

or equivalently

$$\rho = Q\,\sigma^F\,. \tag{8}$$

From fundamental thermodynamics, the adiabatic index is

$$\gamma = 1 + \frac{2}{F}\,. \tag{9}$$

The quantity s is a pseudo-entropy: it is spatially constant for a well-mixed adiabatic system (as this paper assumes). The laxer constraint of convective stability would require that $\mathrm{d}s/\mathrm{d}r \geq 0$ everywhere. The related value $Q = s^{-F/2}$ is a generalized phase-space density. The halo's total mass and outer radius can be finite if $-2 < F < 10$. An SIDM phase or process with $F < 0$ would ensure a flat, accelerating cosmology (obviating dark energy, e.g. Bento, Bertolami & Sen 2002; Kleidis & Spyrou 2015) but the self-bound haloes would be denser outside than in their centres.

The physical meanings of F in various contexts were discussed in Saxton & Wu (2008), Saxton & Ferreras (2010), Saxton (2013), and Saxton et al. (2014). The equations (7) and (8) might describe an SIDM fluid in adiabatic conditions (which is appropriate for a non-reactive, non-radiative, and pressured entity). For example, if DM has composite bound states (e.g Kaplan et al. 2010; Boddy et al. 2014; Cline et al. 2014b; Wise & Zhang 2014; Choquette & Cline 2015; Hardy et al. 2015) that include dark molecules, then $F > 3$. Alternatively, F might just as well describe the scalar field of Peebles (2000), where F derives from a self-coupling term in the particle Lagrangian. Polytropic conditions also occur if the Tsallis thermostatistics apply to collisionless self-gravitating systems (Tsallis 1988; Plastino & Plastino 1993; Nunez et al. 2006; Zavala et al. 2006; Vignat, Plastino & Plastino 2011; Frigerio Martins, Lima & Chimenti 2015). It is conceivable that F varies between astrophysical environments: e.g. due to phase changes; dark molecule formation/dissociation; or the transition to the relativistic regime of a dark fermion gas (Arbey 2006; Slepian & Goodman 2012; Cline et al. 2014a; Domcke & Urbano 2015). These complications depend on specific detailed microphysical models, so for this paper we prefer to focus on the ideal of uniform F, and explore the generic consequences of low- and high-heat capacities.

The quantity $\sigma \equiv \sqrt{P/\rho}$ is analogous to the Newtonian 1D velocity dispersion (assumed to be isotropic). It is however possible that $\sigma > c$ in sufficiently hot regions. The adiabatic sound speed u is given by (Tooper 1965)

$$u^2 = c^2\,\frac{\partial P}{\partial\rho}\Big/\frac{\partial\epsilon}{\partial\rho} = \frac{\gamma\sigma^2 c^2}{c^2 + \frac{F}{2}\gamma\sigma^2}\,. \tag{10}$$

[2] Many papers use a different 'polytropic' law, $P \propto \epsilon^\gamma$ (e.g. Zurek & Page 1984; de Felice, Yu & Fang 1995). This leads to some simpler results, but is harder to interpret in terms of microphysical heat capacity. Our version describes truly adiabatic conditions, and prevents unphysical outcomes such as superluminal or subzero sound speeds. Mrázová, Hledík & Stuchlík (2005) compare these assumptions further.

This is always subluminal if $F \geq 2$. The maximal sound speed is less if the heat capacity is greater[3] ($u \leq c\sqrt{2/F}$). The radial propagation time for sound waves and light is given by

$$\frac{\mathrm{d}t_{[\mathrm{s,l}]}}{\mathrm{d}r} = \frac{\mathrm{e}^{-\Phi}}{[u,c]}\sqrt{\frac{r}{r-h}}\,. \tag{11}$$

Pressure profiles in particular solutions obtained from (2) and (4) are steep and sensitive to F, while the radial profiles of σ^2 are more gently varying. For this practical reason, we solve gradient equations for σ^2,

$$\frac{\mathrm{d}\sigma^2}{\mathrm{d}r} = -\frac{2G}{F+2}\frac{(m+4\pi r^3 Q\sigma^{F+2}/c^2)}{r(r-h)}\left(1+\frac{F+2}{2}\frac{\sigma^2}{c^2}\right), \tag{12}$$

and find P and ρ in post-processing using equations (7) and (8). Relations (3), (5), and (12) imply

$$\Phi = \frac{1}{2}\ln\left(1-\frac{2GM}{c^2R}\right) + \ln\left(\frac{2c^2}{2c^2+(F+2)\sigma^2}\right). \tag{13}$$

The gravitational redshift relative to an observer at infinity ($z = \mathrm{e}^{-\Phi} - 1$) thus depends on local σ and surface boundary conditions. Evidently, $\Phi \to -\infty$ at any point where $\sigma \to \infty$. With locally infinite redshift, the dt term vanishes from the interval (1). Time is frozen at this surface, and the surrounding structure is long-lasting (indeed eternal) to outside observers. This inner surface is a non-rotating naked singularity in a density spike, settled without ongoing inflow. In limiting cases, where $r \to h$, it becomes an event horizon too. We describe these conditions further in subsection 3.2.

2.2 Numerical integration

To obtain a solution for the radial profile, we may start at the outer boundary ($r = R$), where we set the total mass ($m = M$) and vacuum conditions ($\rho = 0$, $\sigma = 0$). The degrees of freedom (F) and phase-space density (Q) are chosen constants. The ordinary differential equations (ODEs) for each quantity y are used in the forms $\mathrm{d}y/\mathrm{d}\sigma^2$, $\mathrm{d}y/\mathrm{d}r$, or $\mathrm{d}y/\mathrm{d}m$, depending on which gives the shallowest gradients. In the locally appropriate form, the set of ODEs is integrated radially inwards from the preceding reference point using Runge–Kutta methods (RKF45, RK4IMP, and RK8PD in the GNU SCIENTIFIC LIBRARY) until the inner boundary is found: $\sigma \to \infty$ or $m \to 0$, whichever happens first. To initially launch the solver inwards from the outer boundary, the first partial integral is a small radial step using $-\mathrm{d}y/\mathrm{d}r$ ODEs. Then, there are tentative steps using $\mathrm{d}y/\mathrm{d}\sigma^2$ ODEs, while $\sigma^2 < 10^{-2}c^2$. At medium radii, the integrator proceeds using $-\mathrm{d}y/\mathrm{d}\ln r$ ODEs, picking tentative target radii cautiously outside the local Schwarzschild value (h). If this process becomes slow due to steep gradients when $r \to h$, the integrator swaps to another choice of independent variable, and proceeds in terms of $\mathrm{d}y/\mathrm{d}\sigma^2$ or $\mathrm{d}y/\mathrm{d}m$ ODEs. Eventually the numerical integral halts at an impassable inner boundary. There are two possible types.

In many cases, the gradient of σ^2 steepens at small r, and the temperature and density blow up, inevitably to form a sharp inner boundary. Approaching that limit, it is informative to rewrite the differential equations as

$$\frac{\mathrm{d}r}{\mathrm{d}\ln\sigma^2} = -\left(\frac{F+2}{2}\right)\frac{r(r-h)c^2\sigma^{-(F+2)}}{GD\left(c^2\sigma^{-2}+\frac{F+2}{2}\right)}, \tag{14}$$

$$\frac{\mathrm{d}m}{\mathrm{d}\ln\sigma^2} = -\left(\frac{F+2}{2}\right)\frac{4\pi r^3(r-h)Q}{GD}\left(\frac{c^2\sigma^{-2}+\frac{F}{2}}{c^2\sigma^{-2}+\frac{F+2}{2}}\right), \tag{15}$$

$$D \equiv m\sigma^{-(F+2)} + 4\pi r^3 Q/c^2\,. \tag{16}$$

As $\sigma^2 \to \infty$, the derivative $\mathrm{d}r/\mathrm{d}\ln\sigma^2 \to 0$ (meaning that temperature and density rise sharply over a tiny radial step inwards). The mass derivative $\mathrm{d}m/\mathrm{d}\ln\sigma^2$ approaches a constant asymptotically. A thin dense inner shell, where σ^2 rises by a ratio $\sim\exp(2Gm/Fc^2r)$, can account for most of the remaining inner mass. These are singular profiles.

If, in other cases, the density gradient becomes shallow at small r, then the inner mass $m \sim 4\pi r^3\rho/3$, and the potential gradient $\mathrm{d}\Phi/\mathrm{d}r \propto r$ flattens. This self-consistently compels the gradients of ρ, σ^2, and P to flatten towards the centre. Such solutions are non-singular. In those cases, another integration method determines the radial profile more directly. We set non-singular conditions at the origin: $r = 0$, $m = 0$, and positive values of σ^2 and Q. Integration proceeds outwards adaptively in small steps, using the $\mathrm{d}y/\mathrm{d}r$, $\mathrm{d}y/\mathrm{d}m$, and $-\mathrm{d}y/\mathrm{d}\sigma^2$ equations, until nearing the outer boundary $\sigma^2 \to 0$. Iteration of trial steps in dr or direct integration to the limit in $-\mathrm{d}\sigma^2$ yields the outer boundary conditions (R, M, etc.). By construction, this method never finds any of the singular solutions.

Throughout the numerical integrals, our solver routines keep the relative error on each variable within 10^{-11}. The code records all variable states at intermediate radial shells in an ordered data structure, which provides checkpoints for retrospective refinements. Finally, the inner boundary conditions are recorded ($r_\dagger$, $m_\dagger$, $\Phi_\dagger$, etc.). With both boundaries identified, we can safely integrate the ODEs inwards or outwards from any checkpoint, to quickly find the conditions anywhere else. We refine the grid recursively around interesting features, e.g. the half-mass radius (R_m); and any radii where the density index ($\alpha \equiv \mathrm{d}\ln\rho/\mathrm{d}\ln r$) is integer. Once the profile is recorded at satisfactory resolution, the solution can be rescaled (e.g. to unit radius $R = 1$) using the innate homologies of the model (Appendix A).

3 RESULTS

3.1 Parameter-space domains

To standardize our description of the parameter space, let us define some global properties of each solution, in terms that are invariant under the model's natural scaling homologies.

The halo's mean density is $\bar{\rho} = 3M/4\pi R^3$ and surface escape velocity is $V = \sqrt{2GM/R}$. As in Saxton et al. (2014), we quantify the gravitational compactness and phase-space density in dimensionless terms:

$$\chi \equiv \frac{V^2}{c^2} = \frac{2GM}{c^2R} \tag{17}$$

$$q \equiv \frac{Q\,V^F}{\bar{\rho}} = \frac{\rho}{\bar{\rho}}\left(\frac{V}{\sigma}\right)^F. \tag{18}$$

Characteristically, $\chi \lesssim 10^{-4}$ for galaxy clusters; $\chi \lesssim 10^{-6}$ for giant galaxies; $\chi \lesssim 10^{-8}$ for dwarf galaxies. These are upper limits

[3] In adiabatic ultrarelativistic media, acoustic waves propagate slower than light or gravity waves. When there are two coterminous relativistic fluids, the lower F medium (e.g. radiation-dominated plasma) conducts sound faster than the high-F fluid (e.g. $F > 6$ forms of DM). This may have consequences in the early Universe. Cyr-Racine et al. (2014) modelled some cosmic dark acoustic oscillations for $F < 6$.

since a small perturbation of the system can spread out a small mass element of the halo fringe, raising R without greatly affecting the core structure. To lessen this sensitivity to the outskirts, we will sometimes specify compactness in terms of the equipotential containing the inner half of the mass, $\chi_{\rm m} \equiv -2\Phi_{\rm m}$ (i.e. $r = R_{\rm m}$ and $\Phi = \Phi_{\rm m}$ where $m(r < R_{\rm m}) = \frac{1}{2}M$). In any case, the halo radius R cannot exceed the separation between neighbouring galaxies. The known cosmic mean density gives a lower bound,

$$\chi \gtrsim 4.67 \times 10^{-9} \left[\Omega_{\rm m} \left(\frac{M}{10^{12}\,{\rm m}_\odot} \frac{H}{1\,{\rm km\,s^{-1}\,Mpc^{-1}}} \right)^2 \right]^{\frac{1}{3}} \qquad (19)$$

which for Hinshaw et al. (2013) cosmic parameters gives $\chi \gtrsim 4.8 \times 10^{-8}(M/10^{12}\,{\rm m}_\odot)^{2/3}$.

Fig. 1 illustrates how the ratio of inner and outer radii ($r_\dagger/R$) depends on q, for fixed (F, χ). The smallest values of q give solutions where $r_\dagger \approx \chi R$ and most of the mass is concentrated near $r_\dagger$. At the opposite extreme ($q \gtrsim 10^3$), the inner and outer radii are comparable ($r_\dagger \approx R$), which does not resemble any astronomical object. An intermediate-q domain contains non-trivial solutions where $r_\dagger \ll \chi R$. If $F \leq 6$ and χ is galaxy-like, then q has one special root $q_1 = q_1(F, \chi)$ where $r_\dagger = 0$.

For models with $6 < F < 10$, the landscape has more features. Across a finite domain of q, there are conditions where $r_\dagger < \chi R$.

This q interval is wider when F is greater or χ is smaller. However, for many galaxy-like (F, χ) choices, there exist *multiple* roots q_n where $r_\dagger \to 0$. These states tend to be more abundant if F is larger (implying high-heat capacity in the matter) or χ is smaller (a less-compact or less-massive astronomical system). Solutions at lower q values tend to appear at quasi-regular logarithmic steps. The higher q_n tend to bunch together. The medium q_n are less regular, or show gaps (e.g. the interval $0.03 \lesssim q < 100$ when $F = 8$ and $\chi = 10^{-8}$).

Taken at fixed χ, there is no obvious first-principles explanation for these patterns and irregularities; the q_n values depend on non-linearities of the TOV model. The topography of this parameter space does however correspond to some features in a recent non-relativistic model that successfully predicts the scaling relation between SMBH and galaxy haloes (Saxton et al. 2014). The higher q_n values crowd around a maximum q that is actually a limit where the halo becomes a non-singular Lane–Emden sphere (lacking a compact central mass). Lower q_n values correspond to the 'valley' solutions of Saxton et al. (2014), where the envelope of DM immediately surrounding a SMBH attains densities comparable to the SMBH itself. The q interval where $r_\dagger < \chi R$ corresponds to a 'plateau' where the non-relativistic model predicted a maximum ratio of SMBH to halo core masses ($m_\bullet/M$) for given half-mass compactness $\chi_{\rm m}$. In the Newtonian halo model, q was a continuum. The quantization of $r_\dagger = 0$ models at discrete q_n values is new to the relativistic version. In this fundamental picture, SMBH formation and growth is a simple and inexorable result of decreasing Q (rising entropy) through any unspecified dissipative processes in the DM halo.

3.2 Radial profiles and their classes

At large radii, where $\sigma \ll c$ and $r \gg h$, each density profile resembles a non-relativistic Lane–Emden sphere (e.g. Lane 1870; Ritter 1878; Emden 1907). Fig. 2 depicts the radial density profiles differing in q_n when $F = 7$, 8, 9 and the half-mass compactness is fixed to $\chi_{\rm m} = 10^{-8}$. The plotted region spans the scales of galaxy haloes ($R \sim 100$ kpc) to galaxy nuclei (a few au). In the outermost fringe, the density declines steeply with radius, $\rho \sim (\Phi_R - \Phi)^{F/2}$.

The fringe surrounds a core of softer density gradients. The core is smaller (relative to R) if F is greater or q is smaller (Saxton et al. 2014). In higher q solutions (low entropy; darker curves in Fig. 2) the core is larger and sharper edged; the central density gradients flatten and may be non-singular at the origin.

For lower q (higher entropy), a power-law density spike occurs inside the core. As q is lowered, the spike gains dominance and the core shrinks in relative radial terms. For very low q, the core is indistinct (lightest curves in Fig. 2), as the spike and outer fringe merge. A strong spike occurs wherever a compact central mass dominates over the fluid's local self-gravity, as in Newtonian 'loaded polytropes' with a point-mass at the origin (e.g. Huntley & Saslaw 1975). A Newtonian spike has a power-law form ($\rho \sim r^{-F/2}$) regardless of whether the fluid distribution is stationary (e.g. Kimura 1981; Quinlan et al. 1995; Saxton et al. 2014) or an accretion flow (e.g. Bondi 1952; Saxton & Wu 2008; Lora-Clavijo et al. 2014). In relativistic regions ($\sigma \gg c$), the spike profile becomes $\rho \sim r^{-2F/(F+2)}$.

For $F > 6$, the spike's locally steep density gradients can in some cases give way to more complicated structures. In spike conditions, $\rho \propto r^\alpha$ (with $\alpha < 0$) and the local mass profile obeys ${\rm d}m/{\rm d}\ln r \propto r^{3+\alpha}$. Wherever $\alpha < -3$, which occurs easily when $F > 6$ and $\sigma < c$, a small radial step inwards accounts for a large jump in mass. This leaves a weaker gravity region inside the spike, and hydrostatic balance ensures locally shallow gradients (small ${\rm d}\rho/{\rm d}r$, i.e. 'core' behaviour) until the steep spike behaviour resumes at much smaller radii. As α undulates radially inwards, the profile is terraced: dense inner cores nest concentrically within outer cores. Density plots can resemble a ziggurat or wedding cake. Mathematically, terracing occurs because the coupling of the first-order ODEs (2) and (12) is equivalent to an oscillatory second-order ODE in α. Such features emerged in the study of non-relativistic polytropes: e.g. the non-singular $F \approx 10$ polytropes of Medvedev & Rybicki (2001), and the $6 < F < 10$ galaxy halo models of Saxton et al. (2014).

In principle, terracing can continue inwards forever. However, once the temperature becomes relativistic, $\alpha > -3$ for all meaningful F, which prevents any more α-undulations. When a relativistic core emerges, it is a unique and final central substructure. As long as the outer boundary is finite, the number of cores is finite. Fig. 3 shows some terraced profiles: their velocity dispersion; enclosed mass; and a score for the strength of relativistic effects. The $F = 7$ example has two cores (left column); the $F = 9$ example has four cores (right column).

Conditions at the inner boundary ($r \to r_\dagger$) complete the classification of radial solutions:

(i) Sometimes $m_\dagger = 0$ at $r_\dagger > 0$, with shallow density gradients and small Φ there. This is a 'vacant core' case (Kimura 1981). Its inner boundary lacks self-consistent support and is unphysical. The implication is that the global mass M within $r = R$ was badly estimated. We discard such profiles. In Fig. 1, vacant core solutions occur at high q near the right border.

(ii) A density singularity can occur at $r_\dagger > 0$, and possess a photon-sphere shadow. If this happens at a place where $m_\dagger > 0$ and $r_\dagger \to h_\dagger$ then we have a black hole. If however $m_\dagger = 0$ then we might call this object a 'black bubble'. The bubble surface is induced by pressure rather than mass concentration.[4] Black bubbles occur at q above the q_n roots; black holes arise in the limit $q \to 0$.

[4] In a Newtonian model, we might expect the dense shell to fall radially inwards (e.g. cold gas shells in some cooling flow models, Saxton & Wu 2008) but the time-frozen relativistic boundary need not evolve (from any external viewpoint).

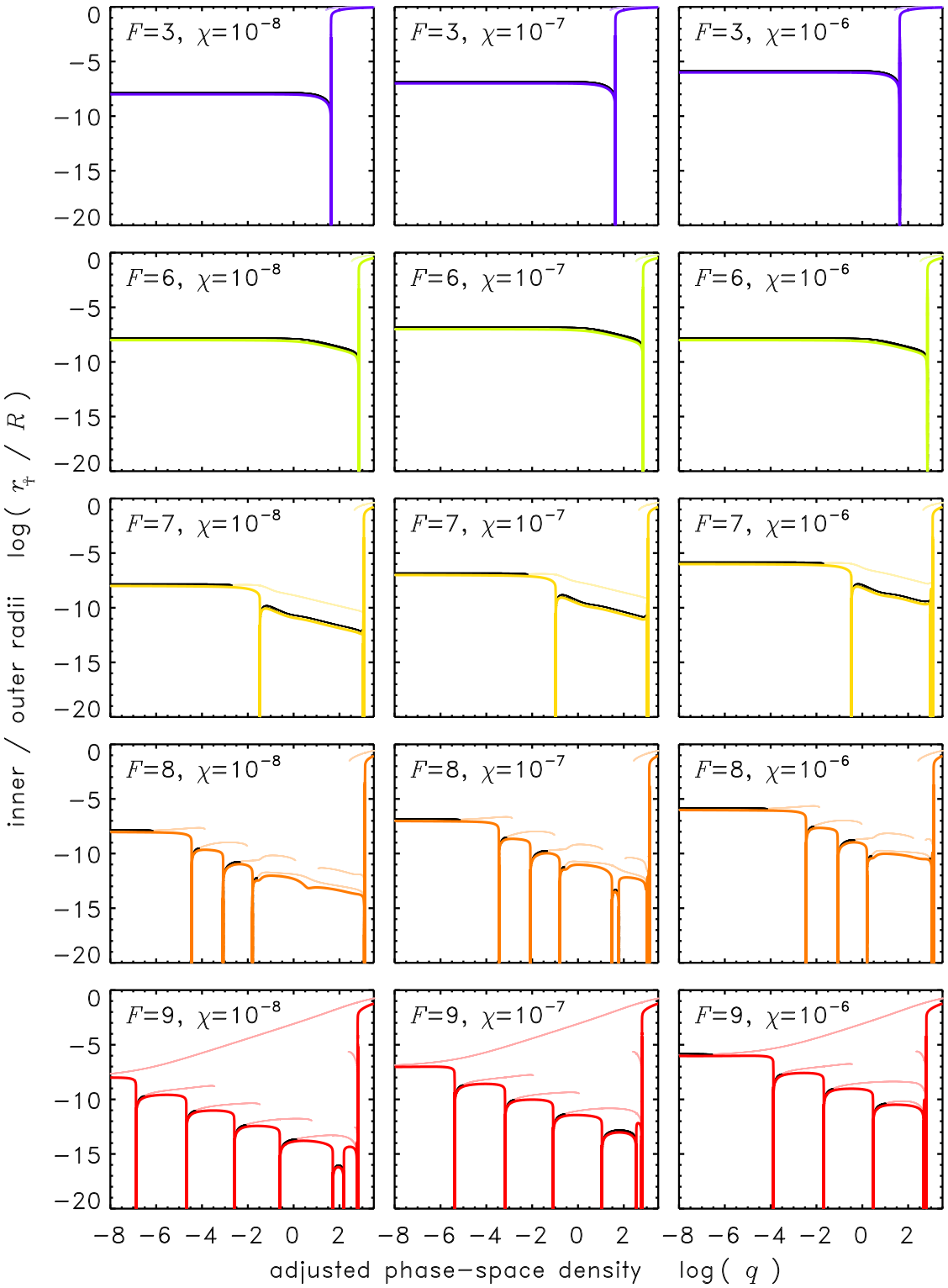

Figure 1. Fractional radii (r/R) as a function of the dimensionless phase-space density q, for equation of state $F = 3, 6, 7, 8, 9$ and halo compactness $\chi = 10^{-8}$, 10^{-7}, 10^{-6} (as annotated in respective panels). Heavy coloured curves show the inner boundary where integration halts ($r_\dagger$). Fainter curves show minima of r/h, including the pseudo-horizon ($r_\bullet$). Black indicates 'photon sphere' surfaces (where present, and derived as in Horvat et al. 2013; Vincent et al. 2015). For large F and small χ, there tend to exist more special states where the horizon or singularity is at the origin (apparent here as sharp downward spikes).

(iii) In special configurations (F, χ, q), the profile is continuous all the way to the origin ($r_\dagger = 0$) and the density gradients are shallow there ($\mathrm{d}\rho/\mathrm{d}r \to 0$). There is no distinct massive central object ($m_\dagger = 0$). This is a non-singular polytropic sphere, resembling TOV toy models of stellar structure. This profile is the only $r_\dagger = 0$ solution when $F \leq 6$ and χ is galaxy-like. For $F > 6$ the largest q_n solution is this type.

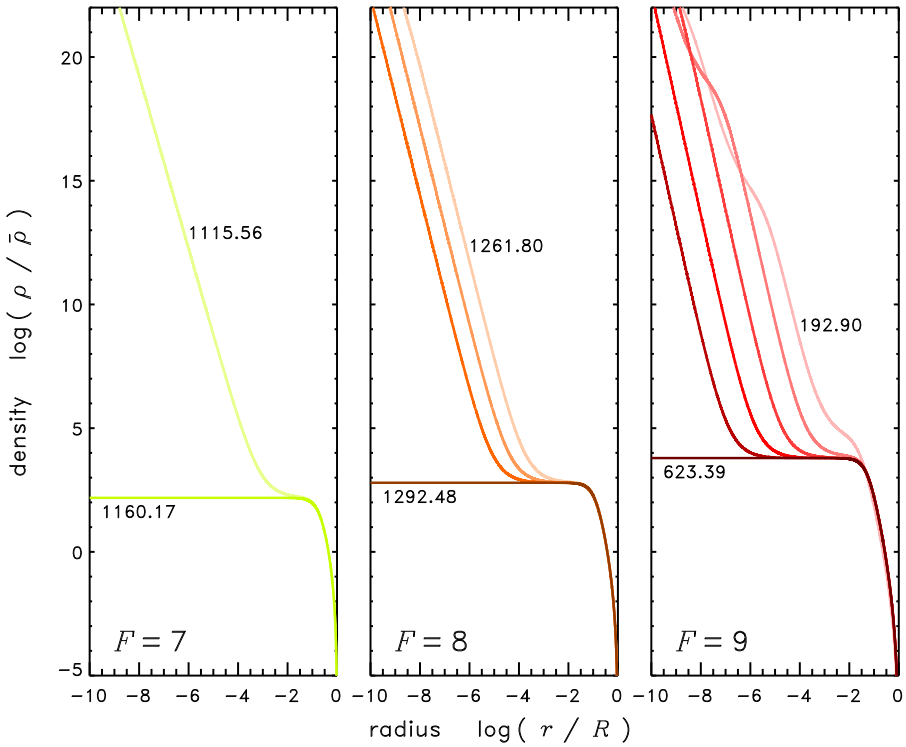

Figure 2. Normalized density profiles, showing halo cores and nuclear spikes, in the $F = 7, 8, 9$ models when the half-mass compactness is $\chi_{\rm m} = 10^{-8}$. From light to dark, the colouring of the curves indicates the order of the q_n values (lowest and highest labelled). For lower q_n (higher entropy), the nuclear spike is radially larger and may overwhelm the core.

(iv) As reported in Section 3.1, for discrete values $q = q_n(F, \chi)$, the density spike can appear at the origin ($r_\dagger = 0$ and $m_\dagger = 0$). This is a non-rotating variety of naked singularity within a pressure-supported envelope.

At given (F, χ), the highest q_n state is non-singular and single-cored. Lower q_n solutions can be terraced or spike-dominated, and are energetically extreme (Appendix B). For each q_n root, there is a non-singular solution and a singular solution, which are alike in their outer profiles; but differ by the presence or absence of a singularity at the origin. This means that a relativistic core is indifferent to whether or not it hosts a BH of much smaller mass.

3.3 Supermassive object & pseudo-horizon

The DM core sizes in observed galaxies and clusters are consistent with $7 \lesssim F \lesssim 9$ (Saxton & Wu 2008; Saxton & Ferreras 2010; Saxton & Wu 2014). With such equations of state, some halo solutions are terraced (at low enough χ and q). In the Newtonian single-fluid context, Saxton et al. (2014) show that a galaxy halo can have a kpc-sized outer core, surrounding a denser inner core or steep spike at subparsec scales. A particularly dense inner core or spike, with locally relativistic σ, might imitate the presence of an SMBH. A true black hole (of much smaller mass) could reside at the centre of this invisible DM envelope. Alternatively, the envelope density can continue gradually rising into a central naked singularity, without any horizon.

The highest q_n eigenvalue gives the simplest central structures. Collectively, we call them the bare solutions. In the non-singular case, there is no distinct central mass, and the inner region is almost uniform. In the highest q_n case containing a singularity, the density rises gradually at smaller radii, without any clear transition between this nuclear spike and the outer halo. Bare solutions represent either: (a) a young or undisturbed galaxy that has not yet formed a nuclear object; or else (b) the nucleus is a naked singularity in a continuous density spike.

Many other solutions feature a layer where r is comparable to the Schwarzschild radius. (i.e. a local dip in the ratio r/h, in the middle row of Fig. 3). We call this place a 'pseudo-horizon' if the ratio is small ($1 < r_\bullet/h \lesssim 10$), and call the profile a loaded model. The object defined by pseudo-horizon radius $r_\bullet$ is a blurry-edged relativistic SIDM ball, enclosing a mass $m_\bullet$. By these definitions, equation (2) implies a condition on the energy density, $4\pi r_\bullet^3 \epsilon_\bullet = m_\bullet c^2$. Outside the pseudo-horizon we find that $mc^2 \gg 4\pi r^3 P$, but not inside. Unlike a BH event horizon, the pseudo-horizon does *not* censor the interior from sight.

For astrophysically relevant choices of the system parameters, the pseudo-horizon typically occurs at $10^{-12} \lesssim r_\bullet/R \lesssim 10^{-7}$. For a galaxy-sized halo ($R \sim 100$ kpc), typical values of $r_\bullet$ correspond to milliparsecs or less. This is compatible with the sizes of observed SMBH candidates (e.g. $r_\bullet \approx 0.08$ au $\approx 4 \times 10^{-7}$pc for Sgr A* in the Milky Way). Fig. 4 shows scatter plots of the central mass fractions $(m_\bullet/M)$ for $7 \leq F \leq 9$ and various compactness (χ). For fixed (F, χ), the sequence of $m_\bullet/M$ verses q_n is 'U'-shaped: the lowest q_n solution has the largest mass $m_\bullet/M$; medium q_n yields smaller $m_\bullet/M$; and the mass fraction rises again with q at the high end. Among the galaxy-like $F = 7$ models shown (e.g. with $\chi \lesssim 10^{-6}$), the central mass is $m_\bullet/M \approx 0.327$ and $m_\bullet/M \lesssim 0.0085$ for small to larger q_n, respectively. For comparable $F = 8$ models, the three lowest q_n solutions have $m_\bullet/M \approx 0.465$, $m_\bullet/M \approx 0.0313$ and $m_\bullet/M \lesssim 0.000\,96$. The four lowest q_n solutions when $F = 9$ have ratios $m_\bullet/M \approx 0.516$, $m_\bullet/M \approx 0.0182$, $m_\bullet/M \lesssim 0.000\,84$, and

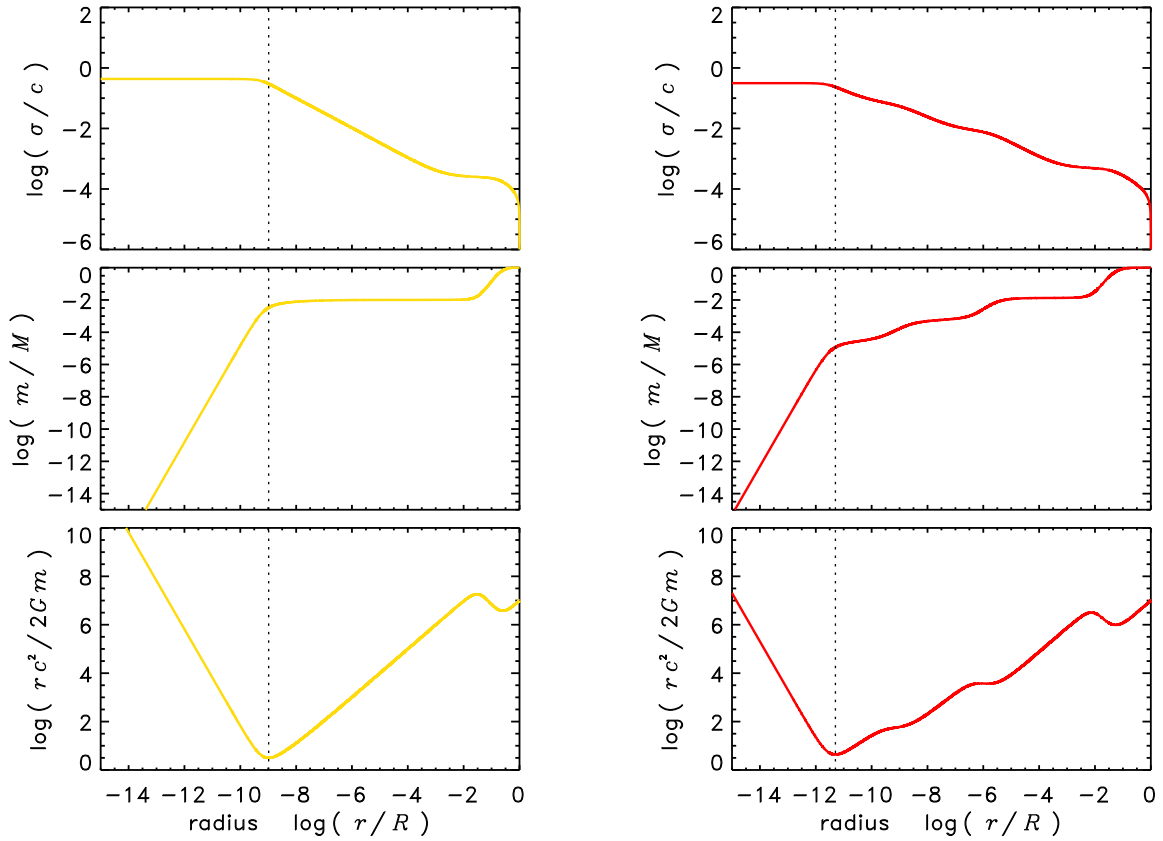

Figure 3. Radial profiles of relativistic polytropes with $(F, \chi, q) = (7, 10^{-7}, 1045.64)$ [left column] and $(F, \chi, q) = (9, 10^{-7}, 353.193)$ [right column]. First row shows thermal velocity dispersion, (σ/c). The second row shows the corresponding profile of the mass enclosed ($m = m(< r)$). The third row shows the ratio of the radius to the local Schwarzschild radius (r/h). Dotted vertical lines indicate the radius of the pseudo-horizon, where the object's size is just larger than the Schwarzschild ideal, i.e. the blurry border separating the central object from its DM envelope and the galaxy halo.

$m_\bullet/M < 0.0003$. Generally for $F > 6$, the lowest q_n solution represents a massive relativistic object under a tenuous and lightweight envelope extending to huge radii. The higher q_n loaded solutions are more compatible with observed SMBH candidates' $m_\bullet$ values.

The central object lacks a truly concealing horizon, and the interior regions are significantly gravitationally redshifted. When light emits from the interior, the ratio of emitted and detected frequencies is $\nu_2/\nu_1 = \sqrt{g_{tt,1}/g_{tt,2}}$, which for the SIDM model gives $g = \nu_\infty/\nu(r) = \exp[\Phi(r)] = 1/(z+1)$ for an intergalactic observer. For the astronomical solutions we have shown, the internal redshift of the central mass ranges from $z \sim 0.1$ up to $z \gtrsim 4.5$. The higher redshift region around the singularity (if present) is only a tiny subvolume, orders of magnitude thinner than $r_\bullet$. If luminous matter traverses or resides within the supermassive SIDM ball, it will appear mildly to severely dimmed and reddened. The nucleus is less a black hole than a gloomy red pit. Comparable but milder gravitational redshifts were derived for non-singular supermassive 'boson star' models (e.g. $z \leq 0.687$, Schunck & Liddle 1997). For each F there is a unique naked singularity solution, with infinite central redshift in a power-law density spike (see Appendix C).

Fig. 5 illustrates the radial profiles immediately surrounding the pseudo-horizon, in families of models that have identical (F, χ) but different q. These curves have been rescaled to pseudo-horizon units ($r_\bullet$ and $m_\bullet$). We omit the bare solutions, since they lack a pseudo-horizon ($m_\bullet = 0$). Many solutions come in pairs that have congruent profiles around the central object, but differing profiles in the galaxy fringe. Pairs include a low-q and high-q solution. In the Figure, many of the low-q profiles (faint shaded) overlap a high-q counterpart (dark dashed curves). In the rich family of solutions for $(F, \chi) = (8, 10^{-7})$, there are three pairs plus two unique solutions at medium q_n. The velocity dispersion σ inside the pseudo-horizon is almost identical for paired solutions, and unequal for unrelated solutions.

At fixed global compactness χ, the supermassive objects tend to have shallower internal potential $\Phi_\bullet$ if F is larger. Within each (F, χ) family, the extreme (low-q and high-q) loaded solutions have:

(i) the weakest pseudo-horizon (larger r/h at the dip);
(ii) shallower interior potential ($\Phi_\bullet$) and weaker redshift;
(iii) steeper decline in ρ just outside $r_\bullet$;
(iv) the dark envelope within $r < 10r_\bullet$ is less massive compared to the central object ($m_\bullet$).

Conversely, the medium-q models have:

(i) the strongest pseudo-horizon (smaller r/h at the dip);
(ii) a deeper interior potential ($\Phi_\bullet$) and stronger redshift;
(iii) a fuzzier outer density profile, with less distinction between the central object and its envelope;
(iv) the dark envelope within $r < 10r_\bullet$ is more massive compared to $m_\bullet$.

A proportionally more massive dark envelope will induce stronger deviations from Schwarzschild predictions for light-bending and circumnuclear orbital motions. A smaller value of $r_\bullet/h$ and deeper potential imply a sharper transition between the interior and exterior,

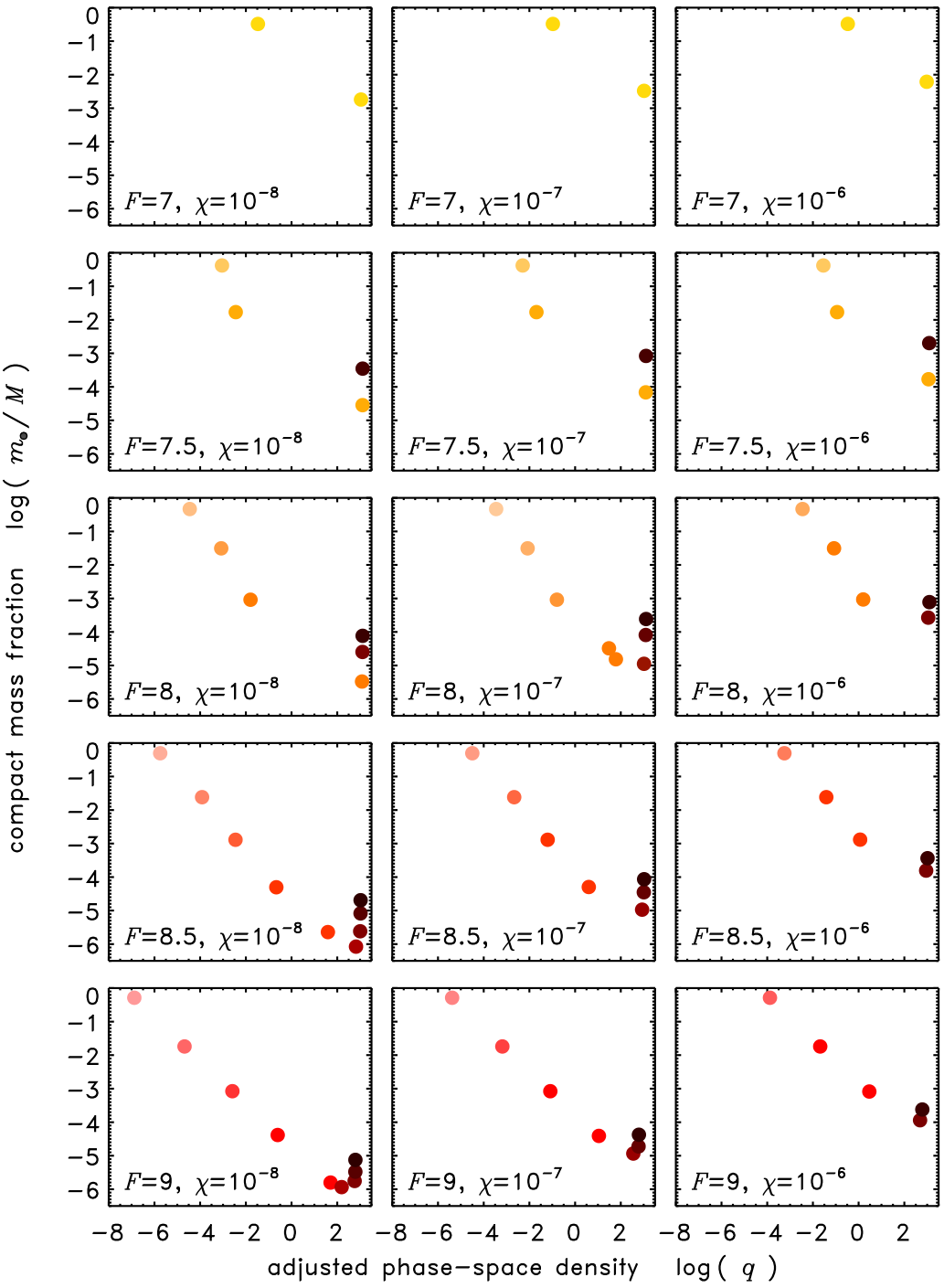

Figure 4. Mass of the central object ($m_\bullet$) compared to the system mass M, for model solutions that have a pseudo-horizon around a distinct central object. Each panel is a different choice of (F, χ) as annotated. We omit the largest q solutions and $F \leq 6$ cases, since they each lack a pseudo-horizon. The dots' hues indicate F, and the darkness is indicates ranking of the q values.

so that the object might be harder to distinguish from a black hole observationally.

The innermost individually observed stars in the Milky Way pass the centre no closer than $r \approx 1400 r_\bullet$ during 'perimelasma' (e.g. Ghez et al. 2008; Gillessen et al. 2009; Meyer et al. 2012). In this region around most of the models in Fig. 5, especially those with shallow $\Phi_\bullet$, the orbital velocity profiles are effectively Keplerian ($v \sim r^{-1/2}$, calculated as in Appendix D). For the deeper-$\Phi_\bullet$ solutions, mpc- and pc-scale rotation curves are only subtly deviant from Keplerian (no flatter than $v \sim r^{-1/3}$). For fitting imperfectly measured stellar orbits, the steep density profile of a $F > 6$ spike could be intrinsically difficult to distinguish from a point-mass or SMBH. With enough precision, precession effects might reveal the dark envelope, though most papers to date apply only to $F < 6$ spikes or Plummer cored profiles (e.g. Rubilar & Eckart 2001; Schödel et al. 2002; Mouawad et al. 2005; Zakharov et al. 2007, 2010; Iorio 2013; Dokuchaev & Eroshenko 2015). At kpc radii, our model velocity profiles can rise as just expected within the DM core of a galaxy, then flatten and

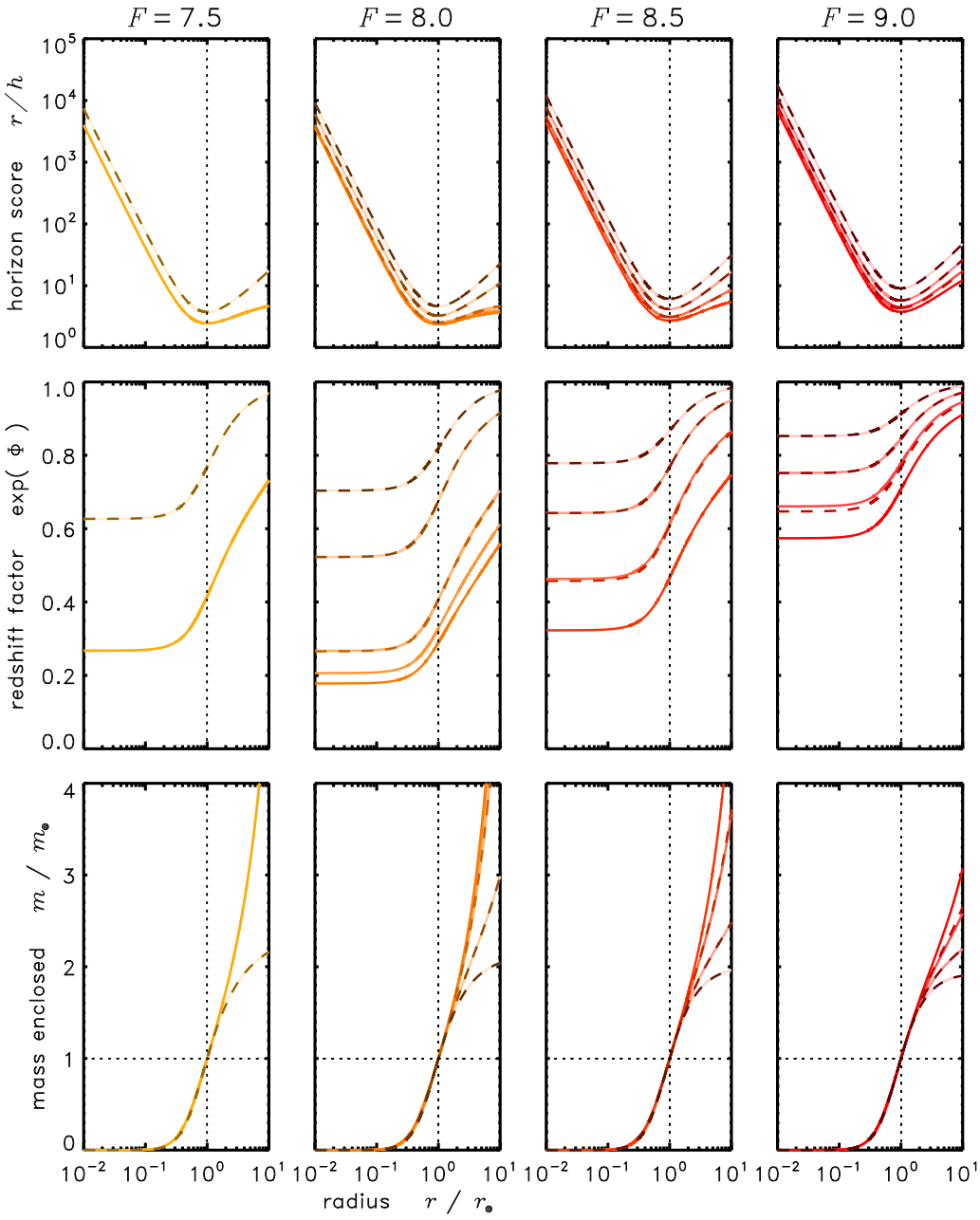

Figure 5. Examples of inner radial structures near the pseudo-horizon of a central object, in several families of halo solutions. Radii and masses are normalized relative to the pseudo-horizon conditions ($r_\bullet$, $m_\bullet$; marked with dotted lines). Each panel shows profiles with different q_n eigenvalues but $\chi = 10^{-7}$ and F fixed as annotated. High-q_n solutions are darker/dashed curves; lower q_n solutions are lighter/solid curves. The top row shows the closeness to Schwarzschild horizon condition: the dip is the pseudo-horizon; a value of $rc^2/2Gm = 1$ would occur at a true horizon. The middle row shows the mass profiles: the dark envelope within $3r_\bullet$ is comparable to the mass of the inner object, and contributes significantly to the space–time bending. The bottom row shows the gravitational redshift factor for any photons escaping the potential to reach distant observers. The redshift is $z = \exp(-\Phi) - 1$. Colours correspond to those in Fig. 4, with darker (dashed) curves for the highest-q solutions, and lighter (solid) curves for lower q.

decline in the outer fringes of the halo. In order to distinguish a central SMBH from a compact SIDM object with a dark envelope, it would be preferable to rely on more direct probes of the $r \lesssim 10r_\bullet$ interior.

4 AN OBSERVATIONAL TEST

The propagation path of light in space–time is bent under gravity and the wavelength is stretched when viewed by a distant observer. Thus, a massive black hole would distort the apparent background stellar surface density around it, casting multiple images of some background stars (Wardle & Yusef-Zadeh 1992; Jaroszynski 1998; Alexander & Sternberg 1999). A massive DM envelope is transparent to light, but it can cause gravitational redshifts and lensing. Its presence around a massive black hole would further complicate the gravitational lensing process. Its sole presence, with a highly dense concentration at the centre of a DM halo, is expected to show observable gravitational effects like those of a black hole, despite the

absence of an event horizon. A dense and massive DM sphere can trap light (Bilić, Nikolić & Viollier 2000; Dabrowski & Schunck 2000; Nusser & Broadhurst 2004; Bin-Nun 2013; Horvat et al. 2013). It can cause light rays to circulate around and also allow them to pass through it, forming an optically scrambled 'photon sphere.'

When star-light is gravitationally lensed, the optical path length to the observer increases. The differing optical path lengths of the rays in multiply lensed variable point-sources behind a deep gravitational well results in differing timing lags in their variable emissions (e.g. Bozza & Mancini 2004). Timing observations therefore provide a useful means to study the properties of space–time around extreme gravity systems, such as black holes, or the dense DM envelopes and spheres described in the previous sections.

Pulsar timing has been identified as a space–time probe because of the high precision achievable in the timing measurements. (e.g. Manchester 2013). It is also because of the unique nature of pulsars (neutron stars) – highly compact (practically a point mass with respect to a massive black hole) and thus uneasily disrupted; narrow mass range; and for millisecond pulsars, high stability in the rotation rate (a stable, reliable clock). Moreover, rotating neutron stars will exhibit various relativistic couplings (see Wex & Kopeikin 1999; Kramer et al. 2004; Pfahl & Loeb 2004; Kocsis, Ray & Portegies Zwart 2012; Liu et al. 2012; Nampalliwar et al. 2013; Remmen & Wu 2013; Angélil & Saha 2014; Singh, Wu & Sarty 2014; Psaltis, Wex & Kramer 2016) that would otherwise be unobservable in the less compact stellar objects. These couplings provide additional handles in the analysis of space–time structures around gravitating objects. Also, there are plausible theoretical reasons to expect swarms of pulsars (and other compact stars) to concentrate in galaxy nuclei (Miralda-Escudé & Gould 2000; Pfahl & Loeb 2004; Freitag et al. 2006). So far, one magnetar is known near Sgr A*, and there is debate about how many pulsars might also be discoverable (Macquart et al. 2010; Wharton et al. 2012; Rea et al. 2013; Bramante & Linden 2014; Dexter & O'Leary 2014; Macquart & Kanekar 2015).

Here, we illustrate how the dynamics of a pulsar (a test particle) responds to the different gravitational fields of polytropic SIDM spheres, and how the radio pulsation properties (i.e. ticks of the clock carried by an orbiting test particle) are affected. Fig. 6 shows the potentials and the gradients of potential of systems with $F = 8$, $\chi = 10^{-7}$, and various q values. The potential and the potential gradient of a Schwarzschild black hole are also shown as a reference. The different potentials give rise to different pulsar orbital dynamics. For a pulsar orbiting around a Schwarzschild black hole, there is a limiting radius within which a stable circular orbit is impossible, i.e. the presence of an innermost stable circular orbit (ISCO). A pulsar would encounter a potential barrier for a central dense polytropic sphere (see Fig. 7, top panel), and hence it can have orbits for all non-zero radii, i.e. an ISCO does not exist. The Keplerian orbital velocity (Ω_k) profiles for the cases of polytropic DM spheres and for the case of a Schwarzschild black hole are different (Fig. 7, bottom panel). In each of these polytropic DM spheres, Ω_k approaches a constant value as the orbital radius decreases.

The differences in gravitational potentials among these cases imply that radiation from an orbiting pulsar is subject to different gravitational redshifts. This frequency shift is a manifestation of time dilation induced by gravity, and the time-dilation factors are thus always larger than one. The radiation from the pulsar is also affected by the pulsar's orbital motion. This is due to the relativistic Doppler effect, not a direct consequence of gravitational effects, and can result in frequency blueshift or redshift, depending on the projected orbital velocity of the pulsar along the line of sight. The

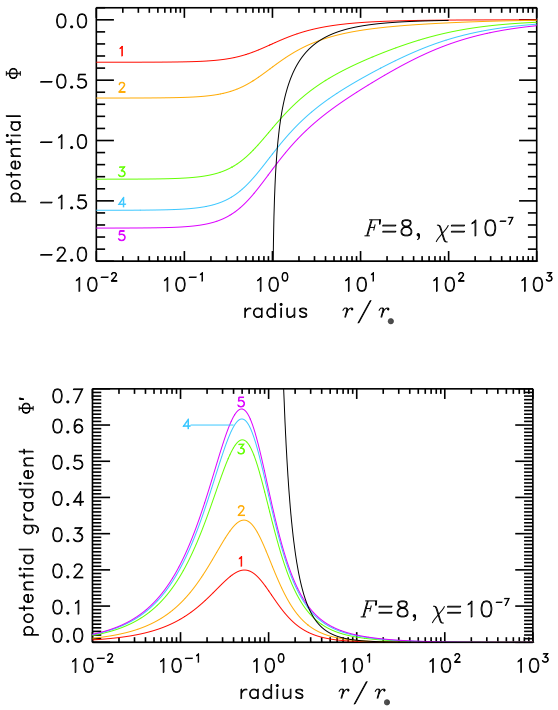

Figure 6. Gravitational potential (top) and gravitational potential gradient (bottom) of polytropic DM spheres with $F = 8$ and $\chi = 10^{-7}$. Curves 1, 2, 3, 4, and 5 correspond to $q = 3.507 \times 10^{-4}$, 8.364×10^{-3}, 1.599×10^{-1}, 3.305×10^{1}, and 6.109×10^{1}, respectively. For reference, the gravitational potential of a Schwarzschild black hole and its gradient (black curves) are also shown in each panel.

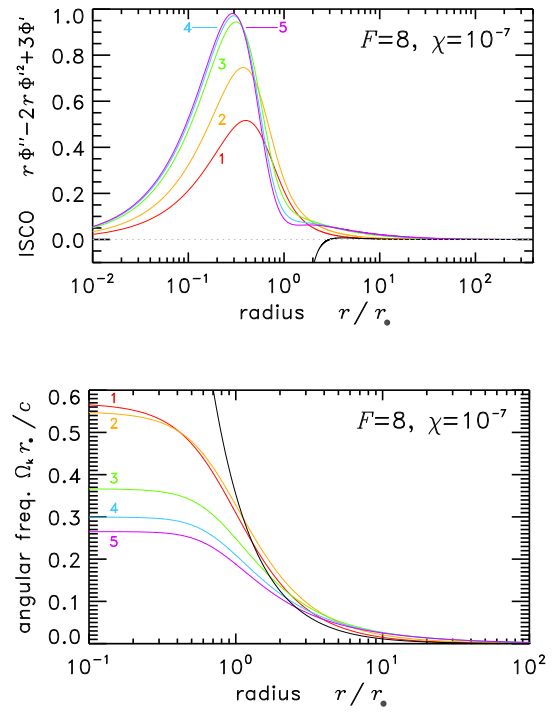

Figure 7. (Top) The ISCO function for different polytropic spheres and a Schwarzschild black hole, as in Fig. 6. A change in sign of this function indicates an ISCO solution (Appendix D). (Bottom) The corresponding Keplerian angular velocity of the polytropic spheres and the Schwarzschild black hole. The same colour/labelling scheme as Fig. 6 is used in both panels.

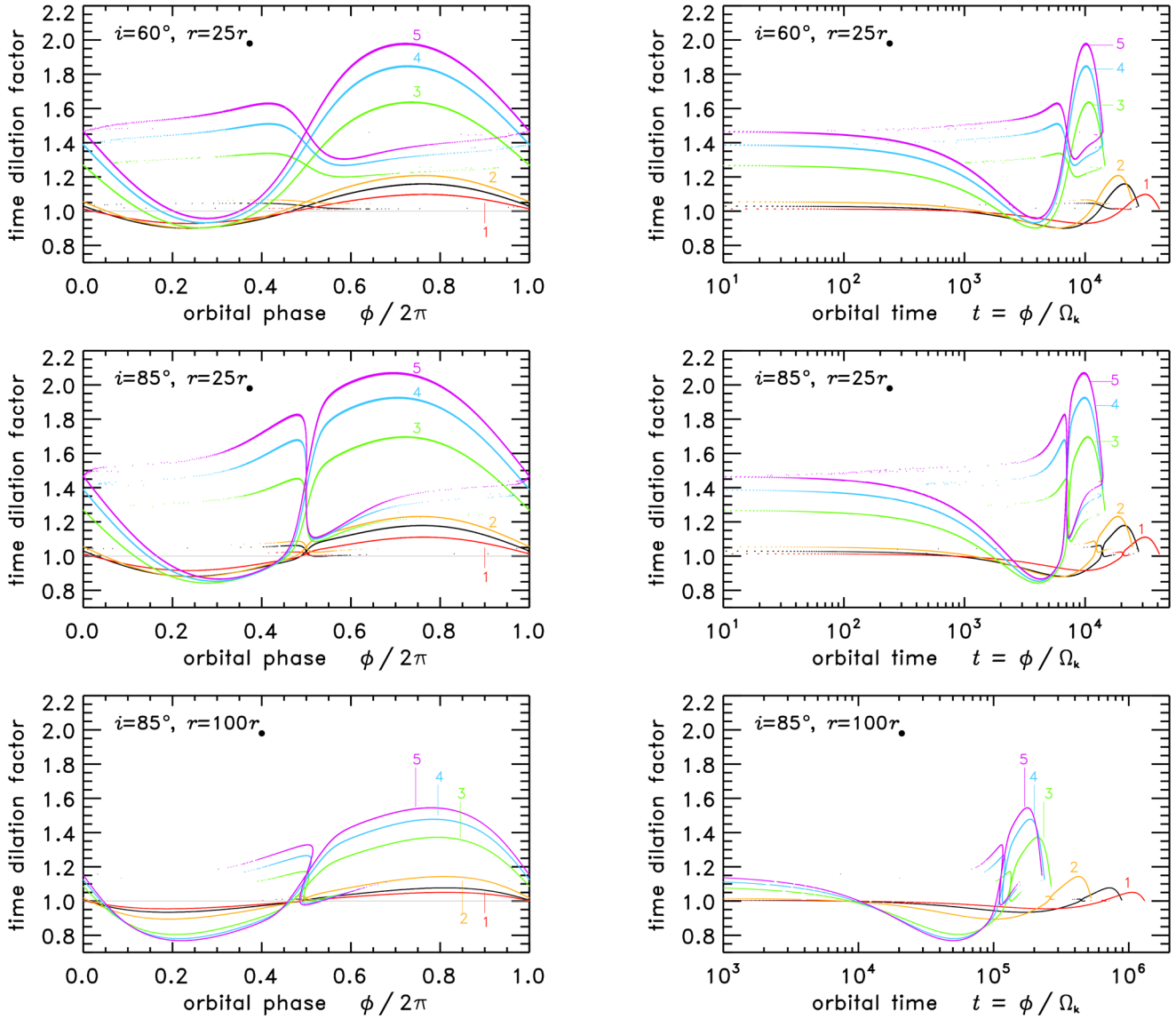

Figure 8. Time-dilation factor of the pulsed radiation from the pulsar located at different ϕ (left column) and time-dilation factor as a function of time as measured by a distant observer (right column) for polytropic DM spheres with $(F, \chi) = (8, 10^{-7})$ as in Figs 6 and 7, compared to a Schwarzschild black hole. Panels from top to bottom in each row correspond to radial distance $r/r_\bullet = 25$, 25, and 100, respectively, and to orbital viewing inclination $i = 60°$, 85°, and 85°, respectively. Multiple, and sometimes dotted, branches of each profile correspond to strongly gravitationally lensed rays which orbit the polytropic DM sphere (or BH) one or more times before reaching the observer.

pulsar's orbital motion is however determined by the gravitational force that confines the pulsar in its orbit, and different gravitational fields will result in different orbital motions. The frequency shift from the pulsar radiation, and hence the apparent modulation of the pulsar's pulse periods as measured by a distant observer, are a combination of the relativistic Doppler shift caused by the pulsar's motion and the time dilation of the radiation that is climbing up a gravitational well (Appendix E). Fig. 8 shows the time-dilation factor of radiation from the pulsar at (i) different azimuthal locations in the orbit and (ii) as a function of time. These calculations are performed using a general-relativistic radiative transfer code (see Younsi, Wu & Fuerst 2012; Younsi & Wu 2015). This factor gives the fractional period variations of the pulses from the pulsar as measured by a distant observer. As shown, the polytropic DM models and the Schwarzschild black hole are distinguishable by measuring the pulsar's orbital period and the variations in the pulse periods across the orbital phases.

Fig. 9 further elaborates the differences between pulse period variations among DM polytropic spheres, by showing the distinctive differences between the pulse period modulations of a pulsar in Keplerian orbits at various radii. In an orbital plane inclined at 85°, each panel illustrates the timing factor at points around circular orbits, for each possible orbit in the radial range $3 \leq r/r_\bullet \leq 25$. The set of concentric pulsar orbits is rendered as if it were a disc, including the gravitational lensing effects. Most noticeably, the shortening of the pulse period (corresponding to frequency blueshift) always occurs when the pulsar orbiting a Schwarzschild black hole is approaching the observer. However, this pulse period shortening is not guaranteed for a DM polytropic sphere when q is sufficiently large. In these cases, the pulse period shortening occurs only when the

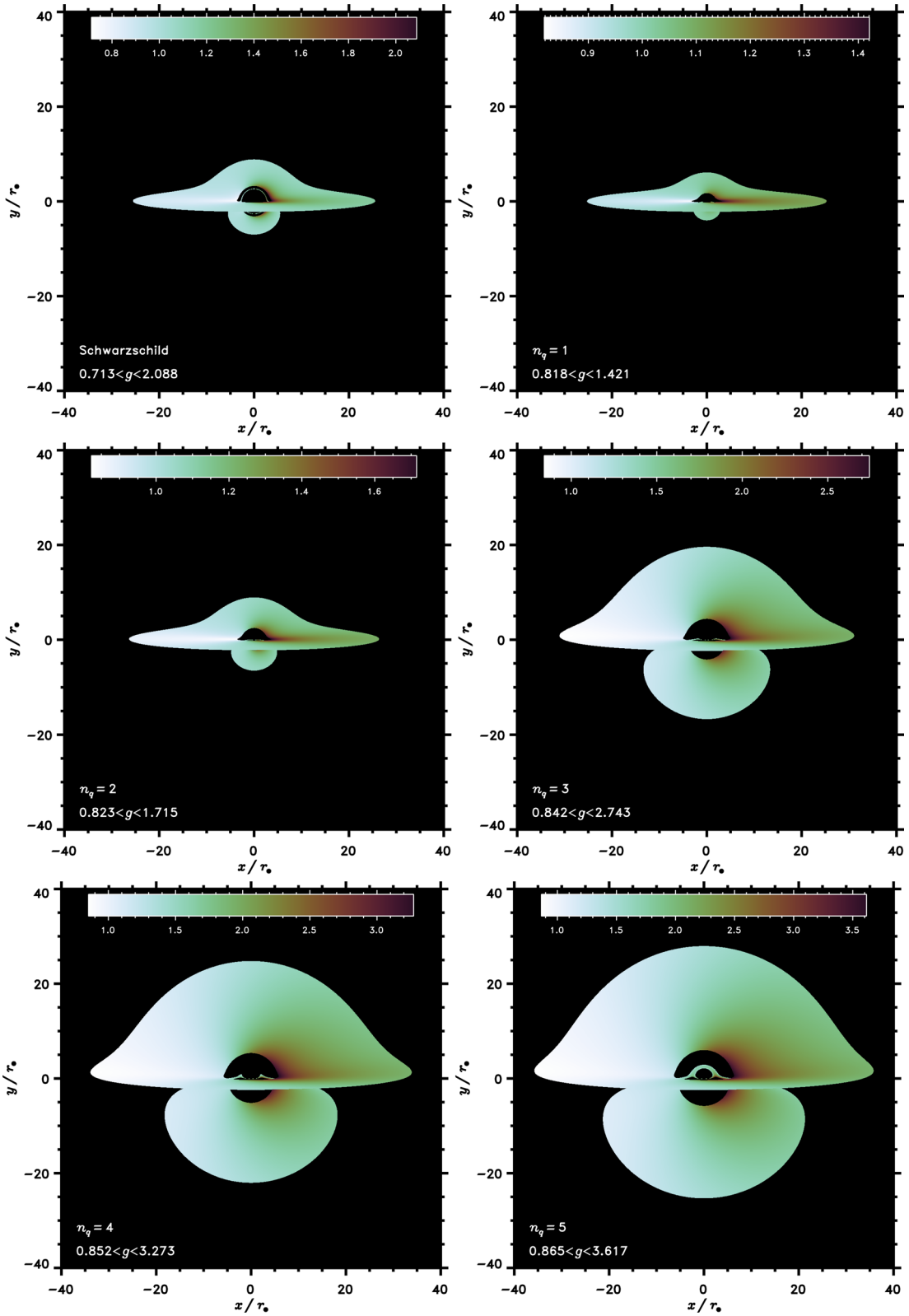

Figure 9. Images showing the time-dilation factor of radiation from a pulsar orbiting on a plane at different locations (radius and azimuthal angle) in the orbit for the polytropic DM model with $F = 8$ and $\chi = 10^{-7}$. The case of a pulsar orbiting around a Schwarzschild black hole is also shown for comparison. The viewing inclination of the pulsar orbit is 85°. From left to right, top to bottom, the images correspond to a Schwarzschild black hole and the polytropic DM sphere with corresponding q values as given by curves 1–5 in Fig. 6, respectively. The axes scale is in units of pseudo-horizon radius (or Schwarzschild radius for the Schwarzschild black hole).

orbit is wide enough that orbital Doppler blueshift dominates the gravitational time dilation. In summary, DM polytropic spheres are distinguishable both amongst themselves and from a Schwarschild black hole via timing observations of the pulsar's pulse period variations and the orbital period.

5 ASTROPHYSICAL IMPLICATIONS

5.1 Accretion of visible matter

Any luminous matter which settles inside the pseudo-horizon appears dimmed, reddened, and time-retarded.

Orbiting stars (and pulsars) can enter and leave the pseudo-horizon. An eccentrically orbiting pulsar that enters and leaves the interior could reveal dramatic timing and spectral variations due to local redshift, regardless of lensing effects. They could also couple to the SIDM tidally. Their gravitational wave emissions will deviate from the ordinary scenario of an SMBH-dominated vacuum. Such coupling was previously predicted for events around massive boson stars (Kesden, Gair & Kamionkowski 2005; Eda et al. 2013; Macedo et al. 2013). The signatures of our SIDM envelope may differ significantly, e.g. because soft high-F fluid has a lower maximum sound speed.

If external tracers lead to an estimated horizon radius $\mathcal{H}$, under a very generic assumption that the object is a black hole, then it is possible that finer observations will reveal internal substructures smaller than $\mathcal{H}$ or flaring events quicker than the time-scale $\mathcal{H}/c$. Observationally, some AGN do show temporal variability on subhorizon scales (e.g. Aleksić et al. 2014). There are also peculiar eruptions in AGN with X-ray lines that appear to be more deeply redshifted than is likely from an SMBH accretion disc (e.g. Bottacini et al. 2015). The X-ray detected flares of some candidates for stellar tidal disruptions seem to imply detonations located at $r < \mathcal{H}$ (Gezari 2012, and references therein). Early VLBI observations indicate luminous structures slightly smaller than the expected shadow of Sgr A* (e.g. Doeleman et al. 2008; Johannsen et al. 2012). These features might be explained by disc and jet events occurring inside a pseudo-horizon (cf. bosonic models, Diemer et al. 2013; Vincent et al. 2015). More mundane explanations could invoke relativistic plasma flows outside a horizon, with compact coruscating bright spots due to beaming; or magnetohydrodynamic shocks and reconnection in the inner jet (e.g. Mizuno 2013; Pu et al. 2015; Younsi & Wu 2015). Distinguishing these possibilities requires spatially resolved images much finer than the horizon size, which could be feasible in the near future. (Note however that a shadow is not definitive proof of a black hole event horizon; Vincent et al. 2015.)

Around black holes in vacuum, there is an ISCO, beyond which the gas from the inner accretion disc is expected to plunge inwards so rapidly that there is little time for it to radiate away its energy. However, the ISCO is absent in many cases with a massive dark envelope, and also when the compact object is a non-singular SIDM ball. This allows the gas to radiate while it gradually flows inwards into the centre of the gravitational well. Subject to Eddington (1918) radiation pressure limits, gas can continue swirling inwards forever, if the inner boundary is singular. The implied radiative efficiency of accretion is therefore higher than for a black hole, though we might expect cooler spectra due to the deep gravitational redshift.

Except the vicinity of a singularity spike, the pseudo-horizon interior has a nearly constant SIDM density, and circular orbits have a uniform period (a classic 'harmonic potential', Binney & Tremaine 1987). If a gaseous accretion disc occupies this region, the lack of differential rotation will allay viscous heating. Without shear and without magnetic flaring, this becalmed zone may be darkened compared to outer annuli of the disc ($r > r_\bullet$). This unhidden but inactive central patch could give the illusion of the central gap due to ISCO in a spinning BH system (e.g. Laor 1991).

Parametric models of a stable compact DM sphere and central singularity, built from an assumed mass profile, have been proposed (Joshi, Malafarina & Narayan 2011, 2014; Bambi & Malafarina 2013), with the (anisotropic) pressure and effective equation of state derived retrospectively. Though these models were not derived from first-principles, they predict accretion disc properties qualitatively similar to those we expect for the polytropic DM model. Detailed modelling of accretion discs in the framework of SIDM models is beyond the scope of this paper, and we leave this exercise to a future study.

5.2 Distortion by visible matter

For the sake of investigating fundamental features, the above-presented models consider idealized spheres of SIDM at rest, without any gravitational influence from other material. We note cautiously that extra constituents could break the model homologies, and perhaps alter some halo features.

DM is apparent in many galaxy centres, as well as the halo. It accounts for several tens of percent of the mass within the half-light radius of elliptical galaxies (Loewenstein & White 1999; Ferreras, Saha & Williams 2005; Thomas et al. 2005, 2007; Bolton et al. 2008; Tortora et al. 2009, 2012; Grillo 2010; Saxton & Ferreras 2010; Bate et al. 2011; Memola et al. 2011; Norris et al. 2012; Grillo et al. 2013; Napolitano et al. 2014; Oguri, Rusu & Falco 2014; Jiménez-Vicente et al. 2015). In theory, the stellar mass distribution can compress the kpc-sized DM core somewhat, compared to DM-only models (e.g. fig. 1 of Saxton 2013).

The inner tens of parsecs of bright galaxies are presumably dominated by visible gas and stars. By conventional assumption, any invisible mass at small radii is attributed to the SMBH (though an unknown portion may actually be dense DM). In stellar dynamical theory, when an SMBH is surrounded by a collisional population of stars, the stellar density evolves a power-law cusp, (e.g. $\rho_\star \sim r^{-7/4}$, Bahcall & Wolf 1976). The compact elliptical galaxy M32 contains one of the densest stellar nuclei known: $\rho_\star > 3 \times 10^7$ m$_\odot$ pc^{-3} and still rising within $r \lesssim 0.4$pc (Lauer et al. 1992; van der Marel et al. 1998). The profile is steep ($\rho_\star \sim r^{-1.5}$) and some kinematic models indicate a heavy central object ($m_\bullet \approx 3 \times 10^6$ m$_\odot$). The centre of the Milky Way also appears cuspy ($\rho_\star \sim r^{-1.85}$), till the density peaks in the nuclear cluster ($\rho_\star \approx 4 \times 10^6$ m$_\odot$ pc^{-3}) and then dips at smaller radii (Becklin & Neugebauer 1968; Kent 1992; Zhao 1996; Figer et al. 2003; Genzel et al. 2003; Schödel et al. 2007; Zhu et al. 2008; Buchholz, Schödel & Eckart 2009; Schödel, Merritt & Eckart 2009). Orbital motions of the innermost stars appear consistent with a dominant compact mass, but may also be consistent with a dark spike within 10 mpc (e.g Mouawad et al. 2005; Zakharov et al. 2007; Ghez et al. 2008; Gillessen et al. 2009; Schödel et al. 2009; Zakharov et al. 2010; Iorio 2013). However, these observations only indicate the total non-luminous mass within the inner stellar orbits, not the partitioning between stellar remnants, the DM spike, and the SMBH or exotic alternative.

The sharp concentration of the stellar cusp in galaxy nuclei might pinch the DM distribution inwards via 'adiabatic contraction', enforcing a DM spike, and perhaps altering traits such as the pseudo-horizon radius $r_\bullet$. Assessing the possible effects on the q_n

roots or SMBH/galaxy scaling relations (Saxton et al. 2014) require detailed multiparameter calculations. Nevertheless, at sufficiently small radii – at least within the innermost star's orbit – the stars cannot directly affect the profile of the central massive object and its dark envelope. Space inside the radius of stellar tidal disruptions by the central object (Hills 1975; Young, Shields & Wheeler 1977; Ozernoi & Reinhardt 1978) will obviously be free of stars. Unless this nuclear environment is dominated by gas, rotation, or swarms of stellar remnants, its inner features should resemble our SIDM-only model.

Luminous gas accumulating *inside* the dark envelope and pseudo-horizon might also become influential. In principle, accumulating baryonic matter could eventually distort the potential towards the limit of SMBH formation (e.g. Lian & Lou 2014). Alternatively, if a compact stellar remnant enters the pseudo-horizon and accretes DM, it might devour the supermassive object from within. This was proposed in the context of supermassive fermion balls (e.g. Munyaneza & Biermann 2005; Richter et al. 2006) and boson balls (e.g. Torres, Capozziello & Lambiase 2000; Kesden, Gair & Kamionkowski 2005). In this way, the supermassive SIDM ball could incubate a seed BH to form a SMBH, predetermining the mass of the final object. This non-luminous growth process evades the Soltan (1982) limit, enabling modern-sized SMBH to arise early in cosmic history.

5.3 Discontinuous halo profiles

Our calculations assume that the pseudo-entropy (s), phase-space density (Q), and degrees of freedom (F) are spatially constant. If the adiabatic fluid were a certain kind of boson condensate then these values could be universal and derivable from the properties of the fundamental particle. In such theories, a universal value of Q could imply a maximum halo mass limit. If however SIDM is a degenerate fermion medium, then Pauli exclusion sets a lower bound on Q, forbidding regions below some line in the (χ, q) plane.

If the halo is a dark fluid, then s and Q are local thermodynamic variables, and could vary spatially. Major galaxy mergers might shock and mix the halo, justifying the uniform-Q assumption. A gentler history (with less mixing) could deposit concentric layers with different (s, Q) values. Buoyant stability requires $\mathrm{d}s/\mathrm{d}r > 0$ and $\mathrm{d}Q/\mathrm{d}r < 0$ everywhere. Stable composite models could embed a high-Q centre under low-Q outskirts, with discontinuities or gradients between. Compared to our homogenous models, stratified haloes could host a smaller compact object than expected from the outer profile.

The universality of the effective degrees of freedom (F) depends on the underlying DM microphysics. Phase changes could alter F suddenly. If the normally large F values are due to bound 'dark molecules', high densities favour more complex bound state formation (increasing F), while high temperatures might favour dissociation ($F \to 3$) near the horizon. Which effect wins is model-dependent. If however the large F were due to DM experiencing extra compact spatial dimensions, then these might remain accessible in all conditions. If the F value derives from a theory like Tsallis thermostatistics, then it might differ from system to system.

5.4 Dark accretion flow and SMBH growth

Our spherical solutions are stationary by construction: hydrostatic pressure supports every layer at rest, all the way down to the origin, or else a bottomless and timeless abyss where $g_{tt} \to 0$. However, quasi-stationary inflow/outflow solutions are also conceivable. If the pressure were raised above the static solution, the halo might excrete unbound DM outwards. If the central pressure were deficient, a contraction and inflow of DM ensues, ultimately accreting from the cosmic background. The accretion rate ($\dot{M}$) could take any value from zero (our hydrostatic profiles) continuously up to the ideal Bondi (1952) rate applicable at the halo surface. Previous self-gravitating GR accretion modelling investigated maximal inflow cases with a 'sonic point' (Karkowski et al. 2006; Kinasiewicz, Mach & Malec 2006; Mach 2009). Over a lifetime $M/\dot{M}$, each instantaneous inflow solution evolves into another case with adjacent (χ, Q).

Our equilibrium profiles share several features with previous models of DM-fed BH growth, with non-relativistic, gravitationally negligible, or collisionless conditions. Spikes appear universally. Gravitational scattering of DM by circumnuclear stars confers a kind of indirect collisionality, producing a fluid-like spike ($\rho \sim r^{-F/2}$ with $F = 3$ for point-like particles) even if the DM theory were collisionless on cosmic scales (Gnedin et al. 2004; Ilyin et al. 2004; Merritt 2004; Zelnikov & Vasiliev 2005; Vasiliev & Zelnikov 2008; Merritt 2010). Models of an SMBH growing by adiabatic accretion of collisionless DM or stars (from an initially uniform background) will also tend to produce this form of spike (Young 1980; Ipser & Sikivie 1987; Quinlan et al. 1995; Gondolo & Silk 1999; Ullio, Zhao & Kamionkowski 2001; MacMillan & Henriksen 2002; Peirani, Kay & Silk 2008). Initially cusped collisionless CDM haloes evolve sharper spikes than an initially cored halo (Quinlan et al. 1995; Gondolo & Silk 1999).

The observation that real SMBH candidates have not overgrown and devoured their host haloes (via runaway DM accretion) may imply that DM is not collisionless and/or the haloes were never cuspy in the first place (MacMillan & Henriksen 2002; Hernandez & Lee 2010). This of course is consistent with SIDM expectations. None the less, in some investigations of BH growth, implicitly or explicitly fluid-like SIDM could contribute significantly (Hernandez & Lee 2010; Pepe et al. 2012). To prevent intermediate mass black holes in globular clusters from growing larger than observed, DM may require sound speeds $>10\,\mathrm{km\,s^{-1}}$ in large galaxy haloes (in the $F = \infty$ model of Pepe et al. 2012). Guzmán & Lora-Clavijo (2011b,a) simulated GR accretion without self-gravity; they found runaway growth from collisionless DM, and minor growth of the SMBH for a fluid with $F \geq 20$. Lora-Clavijo et al. (2014) included self-gravity, and found that SIDM accretion was still only a minor source of SMBH growth. We speculate that a condition with $F < 10$ and more galaxy-like densities might boost DM-fed growth, as in the (Newtonian gas) cooling inflow models of Saxton & Wu (2008, 2014).

Quasi-stationary spherical accretion is not the only possible channel for SMBH growth from SIDM. If the matter is only semifluid, but the mean-free-path is long enough to enable thermal conduction on short cosmic time-scales, then a gravothermal catastrophe might feed the central object. This possibility was explored in spherical time-dependent calculations (Ostriker 2000; Balberg & Shapiro 2002; Balberg et al. 2002; Hennawi & Ostriker 2002; Pollack, Spergel & Steinhardt 2015). In our scenario of fully fluid-like SIDM with $F > 6$, the nuclear spike could be perturbed into a local dynamical collapse, spawning an SMBH directly via 'dark gulping' (in cluster contexts, Saxton & Wu 2008, 2014). The 'skotoseismology' of elliptical galaxies implies collapse modes when the density ratio of stars to SIDM is abnormal (Saxton 2013). These analytically inferred processes await exemplification in non-linear time-dependent simulations.

6 CONCLUSIONS

We self-consistently obtain the equilibrium spherical structures of self-gravitating adiabatic SIDM, from the halo outskirts to the relativistic central region. Low-entropy solutions resemble the cored haloes of primordial galaxies that have not formed a distinct nucleus. There also exist solutions that are pressure-supported all the way down to a fuzzy-edged massive central object or else a naked singularity. For SIDM theories that naturally provide the most realistic core and halo profiles (with thermal degrees of freedom $6 < F < 10$), there exist discretized solutions where the radial origin is exposed.

Among galaxy-like solutions of specified gravitational compactness (χ), the special internal configurations can be labelled by their dimensionless phase-space densities (q), or their entropies.

Some solution profiles have more than one core of near-uniform density, nested concentrically across orders of magnitude in radius. In many models, a dense part of the inner mass profile has a pseudo-horizon, at scales compatible with astronomical SMBH candidates. The relativistic supermassive SIDM ball has interior regions that remain visible from the outside Universe. Gravitational redshifts can reach $z \sim 4.5$ or more, depending on (specific) galaxy properties and the (universal) DM heat capacity. There may be testable consequences. The lack of a perfect horizon means that the effective strong-lensing silhouette of the central structure may differ significantly from SMBH predictions. We present ray-tracing calculations (as described in Younsi et al. 2012; Younsi & Wu 2015) of the timing anomalies of pulsar signals emitted from the vicinity of the central object, which can potentially distinguish these horizonless soft-edged objects from an ordinary SMBH in vacuum.

ACKNOWLEDGEMENTS

CS acknowledges support from the Israel Science Foundation through the astrophysics I-CORE program 1829/12. ZY is supported by an Alexander von Humboldt Fellowship and acknowledges support from the ERC Synergy Grant 'BlackHoleCam – Imaging the Event Horizon of Black Holes' (Grant 610058). Numerical calculations employed mathematical routines from the GNU SCIENTIFIC LIBRARY. This publication has made use of code written by James R. A. Davenport.[5] Specifically, the Fig. 9 colour scheme[6] was modified from one developed by Green (2011). This research has made use of NASA's Astrophysics Data System.

REFERENCES

Ackerman L., Buckley M. R., Carroll S. M., Kamionkowski M., 2009, Phys. Rev. D, 79, 023519
Agnello A., Evans N. W., 2012, ApJ, 754, L39
Aharon D., Perets H. B., 2015, ApJ, 799, 185
Ahn K., Shapiro P. R., 2005, MNRAS, 363, 1092
Aleksić J. et al., 2014, Science, 346, 1080
Alexander T., Hopman C., 2009, ApJ, 697, 1861
Alexander T., Sternberg A., 1999, ApJ, 520, 137
Amorisco N. C., Agnello A., Evans N. W., 2013, MNRAS, 429, L89
Angélil R., Saha P., 2014, MNRAS, 444, 3780
Arabadjis J. S., Bautz M. W., Garmire G. P., 2002, ApJ, 572, 66
Arbey A., 2006, Phys. Rev. D, 74, 043516
Arbey A., Lesgourgues J., Salati P., 2003, Phys. Rev. D, 68, 023511
Babcock H. W., 1939, Lick Obs. Bull., 19, 41
Bahcall J. N., Wolf R. A., 1976, ApJ, 209, 214
Bahcall J. N., Wolf R. A., 1977, ApJ, 216, 883
Balberg S., Shapiro S. L., 2002, Phys. Rev. Lett., 88, 101301
Balberg S., Shapiro S. L., Inagaki S., 2002, ApJ, 568, 475
Bambi C., Malafarina D., 2013, Phys. Rev. D, 88, 064022
Bate N. F., Floyd D. J. E., Webster R. L., Wyithe J. S. B., 2011, ApJ, 731, 71
Becklin E. E., Neugebauer G., 1968, ApJ, 151, 145
Bento M. C., Bertolami O., Sen A. A., 2002, Phys. Rev. D, 66, 043507
Bilić N., Nikolić H., Viollier R. D., 2000, ApJ, 537, 909
Bin-Nun A. Y., 2013, preprint (arXiv:1301.1396)
Binney J., Tremaine S., 1987, Galactic Dynamics. Princeton Univ. Press, Princeton, NJ
Blumenthal G. R., Faber S. M., Flores R., Primack J. R., 1986, ApJ, 301, 27
Boddy K. K., Feng J. L., Kaplinghat M., Tait T. M. P., 2014, Phys. Rev. D, 89, 115017
Bogdán Á., Goulding A. D., 2015, ApJ, 800, 124
Böhmer C. G., Harko T., 2007, J. Cosmol. Astropart. Phys., 6, 25
Bolton A. S., Treu T., Koopmans L. V. E., Gavazzi R., Moustakas L. A., Burles S., Schlegel D. J., Wayth R., 2008, ApJ, 684, 248
Bondi H., 1952, MNRAS, 112, 195
Bonnor W. B., 1958, MNRAS, 118, 523
Bottacini E., Orlando E., Greiner J., Ajello M., Moskalenko I., Persic M., 2015, ApJ, 798, L14
Bottema R., Pestaña J. L. G., 2015, MNRAS, 448, 2566
Bozza V., Mancini L., 2004, Gen. Relativ. Gravit., 36, 435
Bramante J., Linden T., 2014, Phys. Rev. Lett., 113, 191301
Buchholz R. M., Schödel R., Eckart A., 2009, A&A, 499, 483
Buckley M. R., Fox P. J., 2010, Phys. Rev. D, 81, 083522
Burkert A., 1995, ApJ, 447, L25
Burkert A., 2000, ApJ, 534, L143
Burkert A., Tremaine S., 2010, ApJ, 720, 516
Chavanis P.-H., Delfini L., 2011, Phys. Rev. D, 84, 043532
Choquette J., Cline J. M., 2015, Phys. Rev. D, 92, 115011
Cline J. M., Moore G. D., Frey A. R., 2012, Phys. Rev. D, 86, 115013
Cline J. M., Liu Z., Moore G. D., Xue W., 2014a, Phys. Rev. D, 89, 043514
Cline J. M., Liu Z., Moore G. D., Xue W., 2014b, Phys. Rev. D, 90, 015023
Cyr-Racine F.-Y., de Putter R., Raccanelli A., Sigurdson K., 2014, Phys. Rev. D, 89, 063517
de Blok W. J. G., 2010, Adv. Astron., 2010
de Felice F., Yu Y., Fang J., 1995, Class. Quantum Gravity, 12, 739
de Vega H. J., Sanchez N. G., 2014, preprint (arXiv:1401.0726)
Dabrowski M. P., Schunck F. E., 2000, ApJ, 535, 316
Davé R., Spergel D. N., Steinhardt P. J., Wandelt B. D., 2001, ApJ, 547, 574
Destri C., de Vega H. J., Sanchez N. G., 2013, New Astron., 22, 39
Dexter J., O'Leary R. M., 2014, ApJ, 783, L7
Diemer V., Eilers K., Hartmann B., Schaffer I., Toma C., 2013, Phys. Rev. D, 88, 044025
Doeleman S. S. et al., 2008, Nature, 455, 78
Dokuchaev V. I., Eroshenko Y. N., 2015, Sov. J. Exp. Theor. Phys. Lett., 101, 777
Domcke V., Urbano A., 2015, J. Cosmol. Astropart. Phys., 1, 2
Dubinski J., Carlberg R. G., 1991, ApJ, 378, 496
Eda K., Itoh Y., Kuroyanagi S., Silk J., 2013, Phys. Rev. Lett., 110, 221101
Eddington A. S., 1918, ApJ, 48, 205
Elbert O. D., Bullock J. S., Garrison-Kimmel S., Rocha M., Oñorbe J., Peter A. H. G., 2015, MNRAS, 453, 29
Emden R., 1907, Gaskugeln: Anwendungen der Mechanischen Waermetheorie auf Kosmologische und Meteorologische Probleme. Verlag B. G. Teubner, Leipzig
Fabian A. C., Sanders J. S., Haehnelt M., Rees M. J., Miller J. M., 2013, MNRAS, 431, L38
Fan X. et al., 2004, AJ, 128, 515
Feng J. L., Kaplinghat M., Yu H.-B., 2010, Phys. Rev. Lett., 104, 151301
Feoli A., Mancini L., 2009, ApJ, 703, 1502
Ferrarese L., Merritt D., 2000, ApJ, 539, L9
Ferreras I., Saha P., Williams L. L. R., 2005, ApJ, 623, L5
Figer D. F. et al., 2003, ApJ, 599, 1139
Flores R. A., Primack J. R., 1994, ApJ, 427, L1

[5] http://www.astro.washington.edu/users/jrad/idl.html
[6] http://www.mrao.cam.ac.uk/~dag/CUBEHELIX/

Freeman K. C., 1999, in Davies J. I., Impey C., Phillips S., eds, ASP Conf. Ser., Vol. 170, The Low Surface Brightness Universe. Astron. Soc. Pac., San Francisco, p. 3
Freitag M., Amaro-Seoane P., Kalogera V., 2006, ApJ, 649, 91
Frenk C. S., White S. D. M., Davis M., 1983, ApJ, 271, 417
Frigerio Martins C., Lima J. A. S., Chimenti P., 2015, MNRAS, 449, 3645
Gentile G., Salucci P., Klein U., Vergani D., Kalberla P., 2004, MNRAS, 351, 903
Genzel R., Schödel R., Ott T., Eckart A., Alexander T., Lacombe F., Rouan D., Aschenbach B., 2003, Nature, 425, 934
Gezari S., 2012, in EPJ Web Conf., 39, 3001
Ghez A. M. et al., 2008, ApJ, 689, 1044
Ghisellini G., Tagliaferri G., Sbarrato T., Gehrels N., 2015, MNRAS, 450, L34
Gillessen S., Eisenhauer F., Trippe S., Alexander T., Genzel R., Martins F., Ott T., 2009, ApJ, 692, 1075
Gilmore G., Wilkinson M. I., Wyse R. F. G., Kleyna J. T., Koch A., Evans N. W., Grebel E. K., 2007, ApJ, 663, 948
Ginat Y. B., Meiron Y., Soker N., 2016, MNRAS, in press, preprint (arXiv:1603.08886)
Gnedin O. Y., Kravtsov A. V., Klypin A. A., Nagai D., 2004, ApJ, 616, 16
Gondolo P., Silk J., 1999, Phys. Rev. Lett., 83, 1719
Goodman J., 2000, New Astron., 5, 103
Graham A. W., Onken C. A., Athanassoula E., Combes F., 2011, MNRAS, 412, 2211
Green D. A., 2011, Bull. Astron. Soc. India, 39, 289
Grillo C., 2010, ApJ, 722, 779
Grillo C., Christensen L., Gallazzi A., Rasmussen J., 2013, MNRAS, 433, 2604
Gültekin K. et al., 2009, ApJ, 698, 198
Gurevich A. V., Zybin K. P., 1988, Zh. Eksp. Teor. Fiz., 94, 3
Guzmán F. S., Lora-Clavijo F. D., 2011a, MNRAS, 415, 225
Guzmán F. S., Lora-Clavijo F. D., 2011b, MNRAS, 416, 3083
Hardy E., Lasenby R., March-Russell J., West S. M., 2015, J. High Energy Phys., 6, 11
Häring N., Rix H.-W., 2004, ApJ, 604, L89
Harko T., 2011a, Phys. Rev. D, 83, 123515
Harko T., 2011b, MNRAS, 413, 3095
Heikinheimo M., Raidal M., Spethmann C., Veermäe H., 2015, Phys. Lett. B, 749, 236
Hellwing W. A., Barreira A., Frenk C. S., Li B., Cole S., 2014, Phys. Rev. Lett., 112, 221102
Hennawi J. F., Ostriker J. P., 2002, ApJ, 572, 41
Hernandez X., Lee W. H., 2010, MNRAS, 404, L6
Herrmann K. A., Ciardullo R., 2009, ApJ, 705, 1686
Hills J. G., 1975, Nature, 254, 295
Hinshaw G. et al., 2013, ApJS, 208, 19
Hochberg Y., Kuflik E., Volansky T., Wacker J. G., 2014, Phys. Rev. Lett., 113, 171301
Horedt G., 1970, MNRAS, 151, 81
Horiuchi S., Humphrey P. J., Oñorbe J., Abazajian K. N., Kaplinghat M., Garrison-Kimmel S., 2014, Phys. Rev. D, 89, 025017
Horvat D., Ilijić S., Kirin A., Narančić Z., 2013, Class. Quantum Gravity, 30, 095014
Huntley J. M., Saslaw W. C., 1975, ApJ, 199, 328
Iben I., Jr, 1963, ApJ, 138, 1090
Ilyin A. S., Zybin K. P., Gurevich A. V., 2004, Sov J. Exp. Theor. Phys., 98, 1
Inoue S., 2009, MNRAS, 397, 709
Iorio L., 2013, Galaxies, 1, 6
Ipser J. R., Sikivie P., 1987, Phys. Rev. D, 35, 3695
Jaroszynski M., 1998, Acta Astron., 48, 413
Jiménez-Vicente J., Mediavilla E., Kochanek C. S., Muñoz J. A., 2015, ApJ, 806, 251
Jing Y. P., Mo H. J., Börner G., 1998, ApJ, 494, 1
Johannsen T., Psaltis D., Gillessen S., Marrone D. P., Özel F., Doeleman S. S., Fish V. L., 2012, ApJ, 758, 30
Joshi P. S., Malafarina D., Narayan R., 2011, Class. Quantum Gravity, 28, 235018
Joshi P. S., Malafarina D., Narayan R., 2014, Class. Quantum Gravity, 31, 015002
Kadota K., Silk J., 2014, Phys. Rev. D, 89, 103528
Kaplan D. E., Krnjaic G. Z., Rehermann K. R., Wells C. M., 2010, J. Cosmol. Astropart. Phys., 5, 21
Karkowski J., Kinasiewicz B., Mach P., Malec E., Świerczyński Z., 2006, Phys. Rev. D, 73, 021503
Katgert P., Biviano A., Mazure A., 2004, ApJ, 600, 657
Kent S. M., 1992, ApJ, 387, 181
Kesden M., Gair J., Kamionkowski M., 2005, Phys. Rev. D, 71, 044015
Khlopov M., 2014, Int. J. Mod. Phys. A, 29, 1443002
Kimura H., 1981, PASJ, 33, 273
Kinasiewicz B., Mach P., Malec E., 2006, preprint (arXiv:gr-qc/0606004)
Kleidis K., Spyrou N. K., 2015, A&A, 576, A23
Kochanek C. S., White M., 2000, ApJ, 543, 514
Kocsis B., Ray A., Portegies Zwart S., 2012, ApJ, 752, 67
Koda J., Shapiro P. R., 2011, MNRAS, 415, 1125
Kouvaris C., Nielsen N. G., 2015, Phys. Rev. D, 92, 063526
Kovács Z., Harko T., 2010, Phys. Rev. D, 82, 124047
Kramer M., Backer D. C., Cordes J. M., Lazio T. J. W., Stappers B. W., Johnston S., 2004, New Astron. Rev., 48, 993
Lane J. H., 1870, Am. J. Sci. Arts, 2nd ser., 50, 57
Laor A., 1991, ApJ, 376, 90
Laor A., 2001, ApJ, 553, 677
Lauer T. R. et al., 1992, AJ, 104, 552
Lelli F., McGaugh S. S., Schombert J. M., 2016, ApJ, 816, L14
Li C., Jing Y. P., Kauffmann G., Börner G., White S. D. M., Cheng F. Z., 2006, MNRAS, 368, 37
Lian B., Lou Y.-Q., 2014, MNRAS, 438, 1242
Liu K., Wex N., Kramer M., Cordes J. M., Lazio T. J. W., 2012, ApJ, 747, 1
Loeb A., Weiner N., 2011, Phys. Rev. Lett., 106, 171302
Loewenstein M., White R. E., III, 1999, ApJ, 518, 50
Lora V., Just A., Sánchez-Salcedo F. J., Grebel E. K., 2012, ApJ, 757, 87
Lora V., Grebel E. K., Sánchez-Salcedo F. J., Just A., 2013, ApJ, 777, 65
Lora-Clavijo F. D., Gracia-Linares M., Guzman F. S., 2014, MNRAS, 443, 2242
McConnell N. J., Ma C.-P., Gebhardt K., Wright S. A., Murphy J. D., Lauer T. R., Graham J. R., Richstone D. O., 2011, Nature, 480, 215
McCrea W. H., 1957, MNRAS, 117, 562
McDermott S. D., Yu H.-B., Zurek K. M., 2011, Phys. Rev. D, 83, 063509
Macedo C. F. B., Pani P., Cardoso V., Crispino L. C. B., 2013, ApJ, 774, 48
McGaugh S. S., 2012, AJ, 143, 40
McGaugh S. S., Schombert J. M., Bothun G. D., de Blok W. J. G., 2000, ApJ, 533, L99
Mach P., 2009, Rep. Math. Phys., 64, 257
MacMillan J. D., Henriksen R. N., 2002, ApJ, 569, 83
Macquart J.-P., Kanekar N., 2015, ApJ, 805, 172
Macquart J.-P., Kanekar N., Frail D. A., Ransom S. M., 2010, ApJ, 715, 939
Magorrian J. et al., 1998, AJ, 115, 2285
Manchester R. N., 2013, Int. J. Mod. Phys. D, 22, 41007
Medvedev M. V., Rybicki G., 2001, ApJ, 555, 863
Meliani Z., Vincent F. H., Grandclément P., Gourgoulhon E., Monceau-Baroux R., Straub O., 2015, Class. Quantum Gravity, 32, 235022
Melott A. L., Einasto J., Saar E., Suisalu I., Klypin A. A., Shandarin S. F., 1983, Phys. Rev. Lett., 51, 935
Memola E., Salucci P., Babić A., 2011, A&A, 534, A50
Merritt D., 2004, Phys. Rev. Lett., 92, 201304
Merritt D., 2010, preprint (arXiv:1001.3706)
Meyer L. et al., 2012, Science, 338, 84
Miralda-Escudé J., Gould A., 2000, ApJ, 545, 847
Mizuno Y., 2013, ApJS, 205, 7
Moore B., 1994, Nature, 370, 629
Moore B., Gelato S., Jenkins A., Pearce F. R., Quilis V., 2000, ApJ, 535, L21
Mortlock D. J. et al., 2011, Nature, 474, 616
Mouawad N., Eckart A., Pfalzner S., Schödel R., Moultaka J., Spurzem R., 2005, Astronom. Nachr., 326, 83

Mrázová K., Hledík S., Stuchlík Z., 2005, in Hledík S., Stuchlík Z., eds, RAGtime 6/7: Workshops on Black Holes and Neutron Stars. p. 109
Müller Zum Hagen H., Yodzis P., Seifert H.-J., 1974, Commun. Math. Phys., 37, 29
Munyaneza F., Biermann P. L., 2005, A&A, 436, 805
Nampalliwar S., Price R. H., Creighton T., Jenet F. A., 2013, ApJ, 778, 145
Napolitano N. R., Pota V., Romanowsky A. J., Forbes D. A., Brodie J. P., Foster C., 2014, MNRAS, 439, 659
Navarro J. F., Frenk C. S., White S. D. M., 1996, ApJ, 462, 563
Norris M. A. et al., 2012, MNRAS, 421, 1485
Novak G. S., 2013, preprint (arXiv:1310.3833)
Nunez D., Sussman R. A., Zavala J., Cabral-Rosetti L. G., Matos T., 2006, in Pérez M. A., Urrutia L., Villaseqor L., eds, AIP Conf. Proc., Vol. 857, Particles and Fields: X Mexican Workshop on Particles and Fields. Am. Inst. Phys., New York, p. 316
Nusser A., Broadhurst T., 2004, MNRAS, 355, L6
Nusser A., Davis M., 2011, ApJ, 736, 93
Oguri M., Rusu C. E., Falco E. E., 2014, MNRAS, 439, 2494
Oh S.-H., de Blok W. J. G., Walter F., Brinks E., Kennicutt R., 2008, AJ, 136, 2761
Oort J. H., 1932, Bull. Astron. Inst. Neth., 6, 249
Oppenheimer J. R., Volkoff G. M., 1939, Phys. Rev., 55, 374
Ori A., Piran T., 1987, Phys. Rev. Lett., 59, 2137
Ostriker J. P., 2000, Phys. Rev. Lett., 84, 5258
Ostriker J. P., Peebles P. J. E., 1973, ApJ, 186, 467
Ozernoi L. M., Reinhardt M., 1978, Ap&SS, 59, 171
Papastergis E., Adams E. A. K., van der Hulst J. M., 2016, A&A, in press
Peebles P. J. E., 2000, ApJ, 534, L127
Peirani S., Kay S., Silk J., 2008, A&A, 479, 123
Pepe C., Pellizza L. J., Romero G. E., 2012, MNRAS, 420, 3298
Peter A. H. G., Rocha M., Bullock J. S., Kaplinghat M., 2013, MNRAS, 430, 105
Pfahl E., Loeb A., 2004, ApJ, 615, 253
Plastino A. R., Plastino A., 1993, Phys. Lett. A, 174, 384
Pollack J., Spergel D. N., Steinhardt P. J., 2015, ApJ, 804, 131
Postman M. et al., 2012, ApJ, 756, 159
Pota V. et al., 2015, MNRAS, 450, 3345
Psaltis D., Wex N., Kramer M., 2016, ApJ, 818, 121
Pu H.-Y., Nakamura M., Hirotani K., Mizuno Y., Wu K., Asada K., 2015, ApJ, 801, 56
Quinlan G. D., Hernquist L., Sigurdsson S., 1995, ApJ, 440, 554
Rea N. et al., 2013, ApJ, 775, L34
Remmen G. N., Wu K., 2013, MNRAS, 430, 1940
Rhode K. L., 2012, AJ, 144, 154
Richter M. C., Tupper G. B., Viollier R. D., 2006, J. Cosmol. Astropart. Phys., 12, 15
Ritter A., 1878, Wiedemann Ann., 5, 543
Robles V. H., Matos T., 2012, MNRAS, 422, 282
Rocha M., Peter A. H. G., Bullock J. S., Kaplinghat M., Garrison-Kimmel S., Oñorbe J., Moustakas L. A., 2013, MNRAS, 430, 81
Rubilar G. F., Eckart A., 2001, A&A, 374, 95
Salucci P., Burkert A., 2000, ApJ, 537, L9
Salucci P., Wilkinson M. I., Walker M. G., Gilmore G. F., Grebel E. K., Koch A., Frigerio Martins C., Wyse R. F. G., 2012, MNRAS, 420, 2034
Saxton C. J., 2013, MNRAS, 430, 1578
Saxton C. J., Ferreras I., 2010, MNRAS, 405, 77
Saxton C. J., Wu K., 2008, MNRAS, 391, 1403
Saxton C. J., Wu K., 2014, MNRAS, 437, 3750
Saxton C. J., Soria R., Wu K., 2014, MNRAS, 445, 3415
Scharwächter J., Combes F., Salomé P., Sun M., Krips M., 2016, MNRAS, 457, 4272
Schive H.-Y., Chiueh T., Broadhurst T., 2014a, Nat. Phys., 10, 496
Schive H.-Y., Liao M.-H., Woo T.-P., Wong S.-K., Chiueh T., Broadhurst T., Hwang W.-Y. P., 2014b, Phys. Rev. Lett., 113, 261302
Schödel R. et al., 2002, Nature, 419, 694
Schödel R. et al., 2007, A&A, 469, 125
Schödel R., Merritt D., Eckart A., 2009, A&A, 502, 91
Schuberth Y., Richtler T., Hilker M., Salinas R., Dirsch B., Larsen S. S., 2012, A&A, 544, A115
Schunck F. E., Liddle A. R., 1997, Phys. Lett. B, 404, 25
Schunck F. E., Torres D. F., 2000, Int. J. Mod. Phys. D, 9, 601
Schwarzschild K., 1916, Abh. Konigl. Preuss. Akad. Wissenschaften Jahre, 189–196
Scrimgeour M. I. et al., 2016, MNRAS, 455, 386
Shankar F., Weinberg D. H., Miralda-Escudé J., 2009, ApJ, 690, 20
Shapiro S. L., Paschalidis V., 2014, Phys. Rev. D, 89, 023506
Shields G. A., Bonning E. W., 2013, ApJ, 772, L5
Sigurdson K., Doran M., Kurylov A., Caldwell R. R., Kamionkowski M., 2004, Phys. Rev. D, 70, 083501
Singh D., Wu K., Sarty G. E., 2014, MNRAS, 441, 800
Slepian Z., Goodman J., 2012, MNRAS, 427, 839
Soker N., Meiron Y., 2011, MNRAS, 411, 1803
Soltan A., 1982, MNRAS, 200, 115
Spergel D. N., Steinhardt P. J., 2000, Phys. Rev. Lett., 84, 3760
Springel V., Frenk C. S., White S. D. M., 2006, Nature, 440, 1137
Strauss M. A., Ostriker J. P., Cen R., 1998, ApJ, 494, 20
Thomas J., Saglia R. P., Bender R., Thomas D., Gebhardt K., Magorrian J., Corsini E. M., Wegner G., 2005, MNRAS, 360, 1355
Thomas J., Saglia R. P., Bender R., Thomas D., Gebhardt K., Magorrian J., Corsini E. M., Wegner G., 2007, MNRAS, 382, 657
Thomas J., Ma C.-P., McConnell N. J., Greene J. E., Blakeslee J. P., Janish R., 2016, Nature, 532, 340
Tkachev I. I., 1991, Phys. Lett. B, 261, 289
Tolman R. C., 1934, Proc. Natl. Acad. Sci., 20, 169
Tolman R. C., 1939, Phys. Rev., 55, 364
Tooper R. F., 1964, ApJ, 140, 434
Tooper R. F., 1965, ApJ, 142, 1541
Torres D. F., Capozziello S., Lambiase G., 2000, Phys. Rev. D, 62, 104012
Tortora C., Napolitano N. R., Romanowsky A. J., Capaccioli M., Covone G., 2009, MNRAS, 396, 1132
Tortora C., La Barbera F., Napolitano N. R., de Carvalho R. R., Romanowsky A. J., 2012, MNRAS, 425, 577
Tsallis C., 1988, J. Stat. Phys., 52, 479
Tsiklauri D., Viollier R. D., 1998, ApJ, 500, 591
Tully R. B., Fisher J. R., 1977, A&A, 54, 661
Ullio P., Zhao H., Kamionkowski M., 2001, Phys. Rev. D, 64, 043504
Umemura M., Ikeuchi S., 1986, A&A, 165, 1
van den Bosch R. C. E., Gebhardt K., Gültekin K., van de Ven G., van der Wel A., Walsh J. L., 2012, Nature, 491, 729
van der Marel R. P., Cretton N., de Zeeuw P. T., Rix H., 1998, ApJ, 493, 613
Vasiliev E., Zelnikov M., 2008, Phys. Rev. D, 78, 083506
Venemans B. P. et al., 2013, ApJ, 779, 24
Vignat C., Plastino A., Plastino A. R., 2011, Phys. A, 390, 2491
Vincent F. H., Meliani Z., Grandclement P., Gourgoulhon E., Straub O., 2016, Class. Quantum Gravity, 33, 105015
Viollier R. D., Trautmann D., Tupper G. B., 1993, Phys. Lett. B, 306, 79
Vogelsberger M., Zavala J., Loeb A., 2012, MNRAS, 423, 3740
Walker M. G., Peñarrubia J., 2011, ApJ, 742, 20
Wardle M., Yusef-Zadeh F., 1992, ApJ, 387, L65
Wex N., Kopeikin S. M., 1999, ApJ, 514, 388
Wharton R. S., Chatterjee S., Cordes J. M., Deneva J. S., Lazio T. J. W., 2012, ApJ, 753, 108
Wise M. B., Zhang Y., 2014, Phys. Rev. D, 90, 055030
Woo T.-P., Chiueh T., 2009, ApJ, 697, 850
Wu X.-B. et al., 2015, Nature, 518, 512
Xiao T., Barth A. J., Greene J. E., Ho L. C., Bentz M. C., Ludwig R. R., Jiang Y., 2011, ApJ, 739, 28
Yıldırım A., van den Bosch R. C. E., van de Ven G., Husemann B., Lyubenova M., Walsh J. L., Gebhardt K., Gültekin K., 2015, MNRAS, 452, 1792
Yıldırım A. et al., 2016, MNRAS, 456, 538
Yoshida N., Springel V., White S. D. M., Tormen G., 2000, ApJ, 544, L87
Young P., 1980, ApJ, 242, 1232
Young P. J., Shields G. A., Wheeler J. C., 1977, ApJ, 212, 367
Younsi Z., Wu K., 2015, MNRAS, 454, 3283

Younsi Z., Wu K., Fuerst S. V., 2012, A&A, 545, A13
Yu Q., Tremaine S., 2002, MNRAS, 335, 965
Zakharov A. F., Nucita A. A., de Paolis F., Ingrosso G., 2007, Phys. Rev. D, 76, 062001
Zakharov A. F., de Paolis F., Ingrosso G., Nucita A. A., 2010, Phys. At. Nuclei, 73, 1870
Zavala J., Núñez D., Sussman R. A., Cabral-Rosetti L. G., Matos T., 2006, J. Cosmol. Astropart. Phys., 6, 8
Zehavi I. et al., 2002, ApJ, 571, 172
Zelnikov M. I., Vasiliev E. A., 2005, Sov. J. Exp. Theor. Phys. Lett., 81, 85
Zhao H., 1996, MNRAS, 283, 149
Zhu Q., Kudritzki R. P., Figer D. F., Najarro F., Merritt D., 2008, ApJ, 681, 1254
Zurek W. H., Page D. N., 1984, Phys. Rev. D, 29, 628
Zwicky F., 1937, ApJ, 86, 217

APPENDIX A: SCALING HOMOLOGIES

The speed of light c is an absolute scale. All ratios of velocities to c must remain fixed in a homologous transformation of a particular model, and σ^2 is not allowed to rescale within homologous families of models. Therefore, we can only accept rescaling factors

$$X_v = X_\sigma = 1\,. \tag{A1}$$

By dimensional analysis of both sides of the temperature in equation (12), we see that the masses scale in proportion to radial measurements,

$$X_{\rm m} = X_{\rm r}\,. \tag{A2}$$

Dimensional analysis of the polytropic equation of state (7) yields:

$$X_\rho = X_{\rm r}^{-2} \tag{A3}$$

$$X_s = X_{\rm r}^{4/F} \tag{A4}$$

$$X_Q = X_{\rm r}^{-2}\,. \tag{A5}$$

By construction, the dimensionless constants χ and q are invariant under all the valid homology transformations, $X_\chi = X_q = 1$.

APPENDIX B: ENERGETICS AND STABILITY

The energies characterizing each model solution are obtained from supplementary ODEs, solved simultaneously with those for the radial profile (e.g. Iben 1963; Tooper 1964). For diagnostic interest, we record the total mass (M), rest mass (M_0), thermal energy (U), proper energy (E_0) between the inner and outer radii:

$$M = \int_{r_\dagger}^{R} 4\pi r^2 \frac{\epsilon}{c^2}\,{\rm d}r \tag{B1}$$

$$M_0 = \int_{r_\dagger}^{R} 4\pi r^2 \rho \sqrt{\frac{r}{r-h}}\,{\rm d}r \tag{B2}$$

$$U = \int_{r_\dagger}^{R} 4\pi r^2 \frac{FP}{2} \sqrt{\frac{r}{r-h}}\,{\rm d}r \tag{B3}$$

$$E_0 = \int_{r_\dagger}^{R} 4\pi r^2 \epsilon \sqrt{\frac{r}{r-h}}\,{\rm d}r\,. \tag{B4}$$

The total energy of the system is

$$E = Mc^2 = M_0c^2 + U + W = M_0c^2 - B, \tag{B5}$$

where the gravitational potential energy is $W = E - E_0$. Binding energy ($B = -U - W$) refers to the hypothetical initial configuration in which the uncollapsed rest mass was dispersed widely, at zero density and zero pressure. In the absence of detailed mode analyses, a positive binding energy is traditionally interpreted as a sign of secular stability in vacuum conditions, while negative binding energy was seen as a sign of secular instability. We explain below that real stability criteria are not so simple.

In our results for $r_\dagger = 0$ models, the binding energy (relative to a vacuum) is positive for $F < 6$, and negative for $F > 6$. At fixed (F, χ), the magnitude of $|B|$ is greater for the lowest q eigen-models (most concentrated, highest entropy) and lowest for the higher q eigen-models (largest core, lowest entropy). Specifically, the maximum-q solution has binding energy $B \approx [(6-F)/(10-F)]GM^2/R \sim \chi Mc^2$, which is insignificant (in magnitude) compared to the mass–energy of a galaxy-sized object. For $F = 7, 8, 9$, the three lowest q models have large fractional binding energies: $B/Mc^2 \approx -0.074, -0.0592, -0.0297$ (and $B/M_0c^2 \approx -0.080, -0.0629, -0.0306$ in terms of rest mass). Thus, for $F > 6$ haloes, the cored states are low-entropy (primordial?) configurations, and could degrade into singular profiles through dissipative events. However while rising entropy favours concentrated states, binding energy favours the cored states.

Galaxies and clusters with astronomically realistic core sizes and inner mass concentrations may require $6 < F < 10$ (Saxton & Wu 2008; Saxton & Ferreras 2010), which suggests negative binding energies (at least for the dark halo). Can such a structure condense naturally? The real Universe has a positive mean density, $\rho_\infty \equiv \Omega_{\rm m}\rho_{\rm crit} \approx 2.9 \times 10^{-30}\,{\rm g\,cm^{-3}}$ (Hinshaw et al. 2013). This value is a more appropriate reference background than an ideal vacuum. The binding energies of cosmic voids are opposite in sign to self-bound haloes. An initially uniform medium of volume V can differentiate into galaxies and void matter, in some ratio such that $V\rho_\infty c^2 = M_1c^2 + B_1 + M_2c^2 + B_2$ where $B_1B_2 < 0$. In principle, the measurable cosmic fractions of voids and haloes could constrain the effective universal value of F.

While the energy of cosmic voids compensates for haloes forming with $B < 0$, the pressure from the ambient cosmic sea of unbound DM may stabilize galaxies better than in the naïve vacuum assumption. Dynamical stabilization by external pressure is well known in the analogous situation of a gaseous star confined by a dense interstellar medium (e.g. McCrea 1957; Bonnor 1958; Horedt 1970; Umemura & Ikeuchi 1986). In a Newtonian stability condition by Bonnor (1958), the isobaric interface between a radially truncated halo and the external medium must occur within a critical radius ($r_{\rm B}$) where the indicator

$$\delta = -\left[1 - \frac{F-6}{F+2}\frac{Gm^2}{8\pi r^4 P}\right] \Big/ \left[1 - \frac{F-6}{F-2}\frac{m}{4\pi r^3\rho}\right] \tag{B6}$$

changes sign ($\delta > 0$ in unstable outskirts). For our $F > 6$ models with galaxy-like compactness, $r_{\rm B}$ occurs far outside the core, where the density index is steep (bottom panel, Fig. B1) and encloses most of the ideal complete polytrope's mass (always $m_{\rm B} > 0.6M$: top panel, Fig. B1). The ratio $r_{\rm B}/R$ is large for high-q models (cored; low entropy) and the lowest values shown in Fig. B1 are only the extreme low-q cases (sharply concentrated structures). The distribution of the Bonnor limit across polytropes of diverse (χ, q) appears not very sensitive to F, for soft equations of state ($6 < F < 10$).

Surveys and collisionless cosmological theories suggest bulk flows and velocity dispersions of a few hundred ${\rm km\,s^{-1}}$ between galaxies that are not in larger structures (Jing, Mo & Börner 1998;

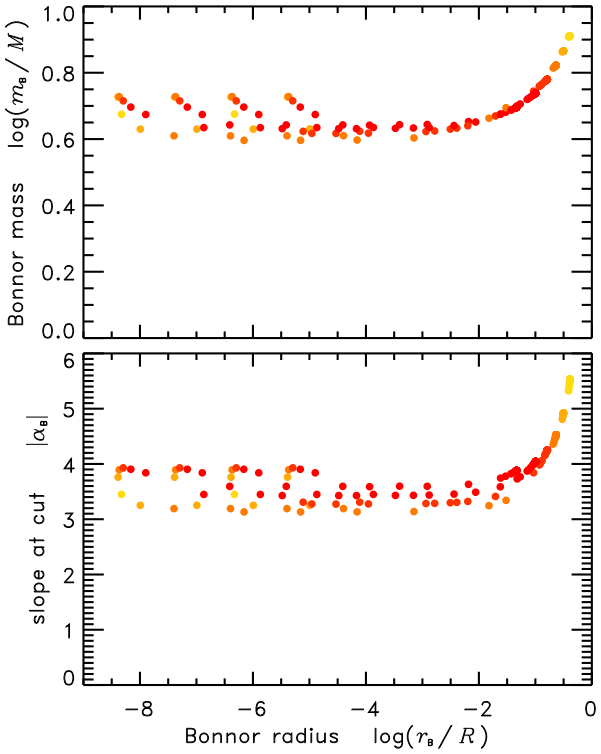

Figure B1. Conditions at the critical radius for Bonnor stability of example models chosen with various global compactness ($\chi = 10^{-6}, 10^{-7}, 10^{-8}, 10^{-9}$) and half-mass compactness ($\chi_m = 10^{-6}, 10^{-7}, 10^{-8}, 10^{-9}$). Colours from yellow to red indicate cases with $F = 7.0, 7.5, 8.0, 8.5, 9.0, 9.5$. The horizontal axis is the ratio of Bonnor-critical radius to the zero-density radius of a complete polytrope (r_B/R). Top panel shows the fractional mass inside the critical radius (m_B/M). Bottom panel shows the logarithmic slope of the halo density profile at r_B.

Strauss, Ostriker & Cen 1998; Zehavi et al. 2002; Li et al. 2006; Nusser & Davis 2011; Hellwing et al. 2014; Scrimgeour et al. 2016). If the intergalactic velocity dispersion (say $\sigma_\infty \approx 300\,\mathrm{km\,s^{-1}}$) is representative of thermal conditions in the unbound SIDM sea, then the cosmic mean pressure ($P_c = \rho_\infty \sigma_\infty^2 \approx 2.2 \times 10^{-15}\,\mathrm{dyncm^{-2}}$) constrains the absolute mass scale of any stable Bonnor-truncated halo model. For a realistic galaxy, truncation must occur well outside the slope-1 radius of the halo core. Fig. B2 depicts the relation between physical values of mass (m_T) and radius (r_T) of Bonnor-stable halo models satisfying this constraint ($R_1 < r_T < r_B$). The occupied swathe of conditions is consistent with observable galaxy masses. The approximate trend is $m_T \propto r_T^2$. Since the peak circular velocity of orbits in the halo is to within some form factor given by $v_{max} \propto \sqrt{G m_T / r_T}$, and if the baryonic fraction varies little among galaxies, then this explains the origin of the observed Tully and Fisher relations, $M \propto v_{max}^4$ (Tully & Fisher 1977; Freeman 1999; McGaugh et al. 2000; McGaugh 2012; Lelli, McGaugh & Schombert 2016; Papastergis, Adams & van der Hulst 2016).

The spherical SIDM-only halo model suffices to describe the interesting basic physics linking the galaxy halo and the relativistic central mass. Including the details of stellar and gaseous components may compress the DM core slightly (subsection 5.2), at the price of a wider parameter space. We expect an enlarged range of stable models. The mingling of the collisionless stellar matter imparts stability in non-singular elliptical galaxies where the SIDM fraction inside the half-light radius is a few tens of percent (Saxton 2013).

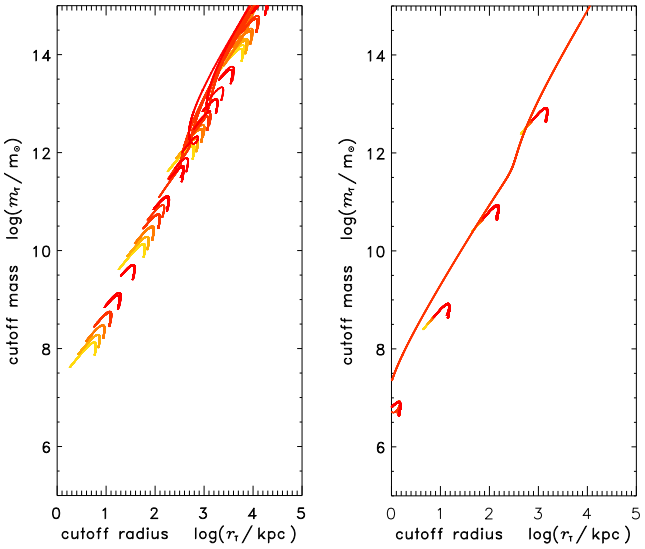

Figure B2. Possible mass and radius, in physical units, of Bonnor-stable truncated haloes, confined by the external pressure of the cosmic SIDM sea. The superimposed loci are derived from many dimensionless models with $F = 7.0, 7.5, 8.0, 8.5, 9.0, 9.5$ (coloured as in Fig. B1) and various values of global compactness ($\log \chi = -6, -7, -8, -9$; left-hand panel) and half-mass compactness ($\log \chi_m = -6, -7, -8, -9$; right-hand panel). Each locus arc shows the possibilities of truncation between the DM core and the Bonnor-critical radius ($R_1 \le r_T \le r_B$).

APPENDIX C: POWER-LAW SINGULARITY

One of the singular solutions ($r_\dagger = 0$) exhibits a simple asymptotic behaviour near the origin. A suitable redefinition of the TOV model in composite variables will ensure finite values everywhere including the origin:

$$\beta_\sigma \equiv \sigma^2 r^{4/(F+2)}, \tag{C1}$$

$$\beta_\rho \equiv \rho\, r^{2F/(F+2)} = Q\, \beta_\sigma^{F/2}, \tag{C2}$$

$$\mu \equiv m/r, \tag{C3}$$

$$\beta_\Phi \equiv \mathrm{e}^\Phi / r. \tag{C4}$$

We choose a logarithmic radial coordinate and rewrite the ODEs:

$$\frac{\mathrm{d}\mu}{\mathrm{d}\ln r} = \frac{4\pi\beta_\rho}{c^2}\left[r^{4/(F+2)} + \frac{F\beta_\sigma}{2}\right] - \mu \tag{C5}$$

$$\frac{\mathrm{d}\beta_\sigma}{\mathrm{d}\ln r} = \frac{4\beta_\sigma}{F+2} - G\frac{\mu c^2 + 4\pi\beta_\rho\beta_\sigma}{c^2 - 2G\mu}\left[\frac{2r^{4/(F+2)}}{F+2} + \frac{\beta_\sigma}{c^2}\right] \tag{C6}$$

$$\frac{\mathrm{d}\beta_\Phi}{\mathrm{d}\ln r} = \beta_\Phi\left[\frac{G(\mu + 4\pi\beta_\rho\beta_\sigma c^{-2})}{c^2 - 2G\mu} - 1\right]. \tag{C7}$$

The inner boundary conditions are

$$\mu_\dagger \equiv \frac{m_\dagger}{r_\dagger} = \frac{4Fc^2/G}{(F+2)^2 + 8F} = \frac{2\pi F Q}{c^2}\,\beta_{\sigma\dagger}^{(F+2)/2} \tag{C8}$$

and $\beta_\Phi > 0$. A similar asymptotic form was implied by de Felice et al. (1995), who assumed a different equation of state ($P \propto \epsilon^\gamma$ in our notation).

In our formulation and calculations, the radial profile can be integrated numerically as an initial value problem, starting at the origin

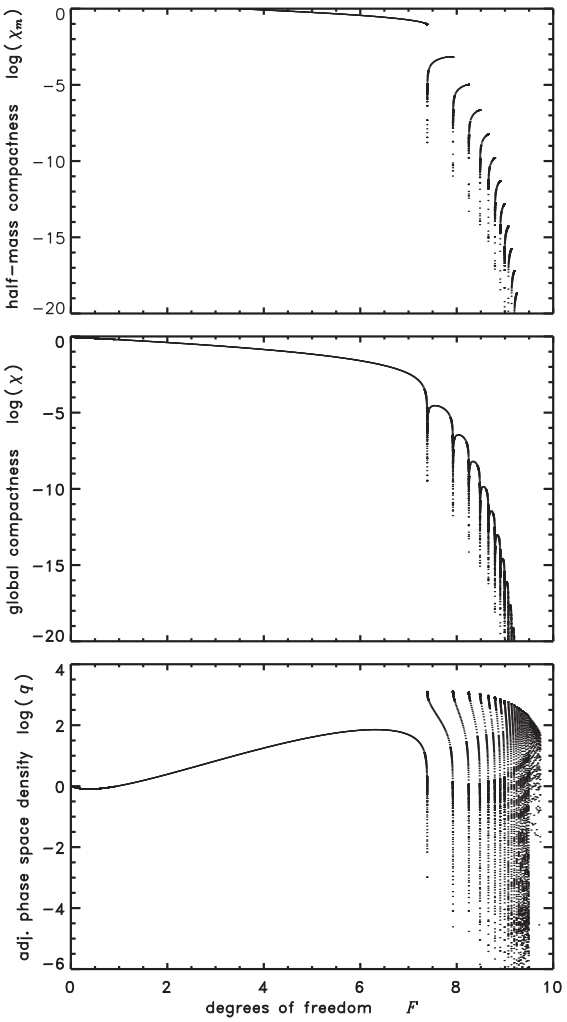

Figure C1. Half-mass compactness (χ_m, top), global compactness (χ, middle), and adjusted phase-space density (q, bottom) of the maximally singular profiles, for various F values.

with a large temperature ($P/\rho c^2 \geq 10^4$) and integrating outwards. When the code reaches a low temperature (e.g. $\beta_\sigma < 10^{-6} r^{A/(F+2)}$), we switch to an integrator in the usual variables and $-\mathrm{d}/\mathrm{d}\sigma^2$ ODEs until the outer boundary limit $\sigma^2 \to 0$. After calculating the full radial profile, the $\beta_\Phi(r)$ values can be normalized retrospectively to match the Schwarzschild outer boundary condition. At given F, there is a unique pair of (χ, q) values consistent with the extreme power-law spike (Fig. C1). When $7 \lesssim F \lesssim 9$, these χ values are compatible with the range of realistic galaxies or clusters, but lower F gives compactness too high, and greater F gives compactness too low (even when measured at the half-mass surface).

The other singular solutions, near the more astronomically relevant (χ, q) eigenvalues, involve a density spike that is steeper than a power law. We do not find any general analytic expressions for those cases. We can only obtain them via numerical integration.

APPENDIX D: ORBITS IN THE ENVELOPE

The motion of the particle is determined by the Euler–Lagrange equation:

$$\frac{\partial \mathcal{L}}{\partial x^\mu} = \frac{\mathrm{d}}{\mathrm{d}\tau}\left(\frac{\partial \mathcal{L}}{\partial \dot{x}^\mu}\right), \tag{D1}$$

where $\dot{x}^\mu \equiv \mathrm{d}x^\mu/\mathrm{d}\tau$. The Lagrangian is given by $\mathcal{L} = g_{\mu\nu}\dot{x}^\mu\dot{x}^\nu$, where $g_{\mu\nu}$ is the space–time metric. For a massless particle $\mathcal{L} = 0$; for a particle with mass we may set $\mathcal{L} = c^2$. Time translational symmetry and rotation symmetry are preserved in a space–time whose metric has no explicit dependence on t and ϕ. This gives the energy and angular momentum conservation conditions:

$$E = c^2 \mathrm{e}^{2\Phi}\, \dot{t}\,, \tag{D2}$$

and

$$L = r^2 \sin^2\theta\, \dot{\phi}, \tag{D3}$$

respectively, where E and L are constants. Conservation of angular momentum implies a planar orbit for the particle. As $\dot{\theta} = 0$, we may set the particle orbit in the $\theta = \pi/2$ plane without losing generality. With these, we can obtain from the Euler–Lagrange equation the equation of motion in the radial direction:

$$(\dot{r})^2 \equiv \left(\frac{\mathrm{d}r}{\mathrm{d}\tau}\right)^2 = \left(\frac{r-h}{r}\right)\left[\frac{E^2\mathrm{e}^{-2\Phi}}{c^2} - \frac{L^2}{r^2} - \mathcal{L}\right]. \tag{D4}$$

The equation can be expressed in terms of an effective potential, $\dot{r}^2 + \mathcal{V}^2 = E^2/c^2$ with

$$\mathcal{V}^2 = \mathcal{A}\mathcal{B} + \frac{E^2}{c^2} \tag{D5}$$

$$\mathcal{A} \equiv \mathcal{L} + \frac{L^2}{r^2} - \frac{E^2\mathrm{e}^{-2\Phi}}{c^2}\,, \tag{D6}$$

$$\mathcal{B} \equiv 1 - \frac{h}{r} = 1 - \frac{2Gm}{c^2 r}\,. \tag{D7}$$

The effective potential has the radial gradients

$$\frac{\partial \mathcal{V}^2}{\partial r} = \mathcal{A}'\mathcal{B} + \mathcal{A}\mathcal{B}' \tag{D8}$$

$$\frac{\partial^2 \mathcal{V}^2}{\partial r^2} = \mathcal{A}''\mathcal{B} + 2\mathcal{A}'\mathcal{B}' + \mathcal{A}\mathcal{B}'', \tag{D9}$$

where we abbreviate $\mathcal{A}' \equiv \mathrm{d}\mathcal{A}/\mathrm{d}r$, $\mathcal{A}'' \equiv \mathrm{d}^2\mathcal{A}/\mathrm{d}r^2$, $\mathcal{B}' \equiv \mathrm{d}\mathcal{B}/\mathrm{d}r$, $\mathcal{B}'' \equiv \mathrm{d}^2\mathcal{B}/\mathrm{d}r^2$, $\Phi' \equiv \mathrm{d}\Phi/\mathrm{d}r$, and $\Phi'' \equiv \mathrm{d}^2\Phi/\mathrm{d}r^2$. In the same notation, the second temporal derivative of the radial motion is $\ddot{r} = -\frac{1}{2}(\mathcal{A}\mathcal{B}' + \mathcal{A}'\mathcal{B})$.

Circular orbits require $\dot{r} = 0$, at a minimum of the potential ($\partial\mathcal{V}^2/\partial r = 0$, $\partial^2\mathcal{V}^2/\partial r^2 \geq 0$). It follows that $\mathcal{A} = 0$ and $\mathcal{A}' = 0$, which give

$$L^2 = \frac{c^2 r^3 \Phi'}{1 - r\Phi'}\,, \tag{D10}$$

$$E^2 = \frac{c^4 \mathrm{e}^{2\Phi}}{1 - r\Phi'}\,. \tag{D11}$$

As L and E are real,

$$r\Phi' < 1\,. \tag{D12}$$

For a stable orbit, $\partial^2\mathcal{V}^2/\partial r^2 \geq 0$. This requires $\mathcal{A}'' \geq 0$ or

$$r\Phi'' - 2r\Phi'^2 + 3\Phi' \geq 0\,. \tag{D13}$$

In a TOV polytrope model,

$$\frac{\Phi''}{\Phi'} \equiv \frac{4\pi r^2\,[\epsilon + (3+\gamma\alpha)P]}{mc^2 + 4\pi r^3 P} - \frac{1}{r} - \frac{\left(1 - 8\pi G r^2 \epsilon c^{-4}\right)}{r - h} \tag{D14}$$

and $\gamma\alpha \equiv \mathrm{d}\ln P/\mathrm{d}\ln r = -r\Phi'(\epsilon + P)/P$.

Moreover, $\epsilon + (3+\gamma\alpha)P = (1 - r\Phi')\epsilon + (3 - r\Phi')P$. Substituting these expressions to eliminate Φ'' from (D13) yields a

more complicated constraint on $r\Phi'$. For any given radius within the spheroid, equation (D10) determines the rotation curve of orbiting stars or accretion disc material. Conditions (D12) and (D13) jointly locate the ISCO.

For a non-circular orbit, $\dot{r} = 0$ occurs when the particle reaches the innermost or outermost radial distance (i.e. the 'perimelasma' and 'apomelasma', respectively) where $A = 0$. At the innermost radial distance $\ddot{r} > 0$ requiring $\mathcal{A}' < 0$; at the outermost radial distance $\ddot{r} < 0$ requiring $\mathcal{A}' > 0$.

APPENDIX E: VARIATIONS IN THE RADIO PULSE PERIOD OF PULSAR

The variations in the period of the radio pulses from a pulsar orbiting a gravitating object are caused by the following two major effects: the Doppler shift due to the pulsar's orbital motion and the time dilation (gravitational redshift) when a radiation pulse propagates up and out of a gravitational well. The two effects are essentially the same effects that cause the frequency shifts of radiation emitted from an object orbiting a gravitating object. As such, we may employ the same ray-tracing technique that is employed in general relativistic radiative transfer calculations.

The first step is to determine the geodesic equations of motion for the pulsar. Here, we do not repeat the basics of determining the motion of particle under gravity, as this subject has already been discussed in Appendix D. We simply present the resultant differential equations directly.

Here and hereafter, an 'overdot' denotes differentiation with respect to the affine parameter and 'primed' variables denote differentiation with respect to the r coordinate. Since the input metric depends on several input parameters which must be interpolated along each geodesic, namely $m(r)$ and $\Phi(r)$ [and their radial derivatives], we make no assumptions of energy or angular momentum conservation along each geodesic. As such, we integrate the following set of four coupled second-order ODEs:

$$\ddot{t} = -2\Phi' \dot{t}\,\dot{r}\,, \tag{E1}$$

$$\ddot{r} = -\Phi' \mathrm{e}^{2\Phi}\left(1 - \frac{2Gm}{c^2 r}\right)\dot{t}^2 + \left(\frac{G}{c^2}\right)\frac{m - r\,m'}{r\left(r - 2Gm/c^2\right)}\dot{r}^2 + \left(r - \frac{2Gm}{c^2}\right)\dot{\theta}^2 + \left(r - \frac{2Gm}{c^2}\right)\sin^2\theta\,\dot{\phi}^2\,, \tag{E2}$$

$$\ddot{\theta} = -\frac{2}{r}\dot{r}\,\dot{\theta} + \sin\theta\cos\theta\,\dot{\phi}^2\,, \tag{E3}$$

$$\ddot{\phi} = -\frac{2}{r}\dot{r}\,\dot{\phi} - 2\cot\theta\,\dot{\theta}\,\dot{\phi}\,, \tag{E4}$$

where $m \equiv m(r)$ and $\Phi \equiv \Phi(r)$.

The non-zero components of the four-velocity of a particle in circular orbit are then given by

$$u^t = \left[\mathrm{e}^{2\Phi}\left(1 - r\,\Phi'\right)\right]^{-1/2}\,, \tag{E5}$$

$$u^\phi = \sqrt{\frac{\Phi'}{(1 - r\,\Phi')\,r\,\sin^2\theta}}\,, \tag{E6}$$

which implies a Keplerian angular velocity

$$\Omega_\mathrm{k} = c\sqrt{\frac{\Phi'\mathrm{e}^{2\Phi}}{r\,\sin^2\theta}}\,. \tag{E7}$$

The fractional variations in the pulsar's radio pulse period are simply the frequency redshift factor of the radiation, which is given by

$$g = \frac{k_\alpha u^\alpha|_\mathrm{emm}}{k_\beta u^\beta|_\mathrm{obs}} = \frac{k_t u^t_\mathrm{emm} + k_\phi u^\phi_\mathrm{emm}}{k_t u^t_\mathrm{obs}}\,. \tag{E8}$$

The two components of the four velocities u^t_emm and u^ϕ_emm are obtained from equations (E5) and (E6), respectively, and $u^t_\mathrm{obs} \equiv \dot{t}_\mathrm{obs}$ is evaluated at the observer's local reference frame. The relevant four-momenta of the photon (radiation) are

$$k_t = -\mathrm{e}^{2\Phi}\dot{t}\,, \tag{E9}$$

$$k_\phi = r^2\sin^2\theta\,\dot{\phi}\,. \tag{E10}$$

This paper has been typeset from a TEX/LATEX file prepared by the author.